Early Growth in a Perturbed Universe: Dark Matter Halo Properties in 2LPT and ZA
Simulations

By

Daniel J. Sissom

Dissertation

Submitted to the Faculty of the

Graduate School of Vanderbilt University

in partial fulfillment of the requirements

for the degree of

DOCTOR OF PHILOSOPHY

in

PHYSICS

August, 2014

Nashville, TN

Approved: Date:

_____   _____
Jocelyn K. Holley-Bockelmann, Ph.D.

_____   _____
Andreas A. Berlind, Ph.D.

_____   _____
David A. Weintraub, Ph.D.

_____   _____
Shane M. Hutson, Ph.D.

_____   _____
Robert J. Scherrer, Ph.D.

ACKNOWLEDGMENTS

This is where you thank the people that made your work possible: grant awarding agencies, advisers, your committee, mom and dad, whatever.

TABLE OF CONTENTS

Page

LIST OF TABLES

LIST OF FIGURES

CHAPTER I

Introduction

Text goes here. This is where we'll talk about the purpose of the project and the layout of this document.

I.1   The Early Universe

Text goes here.

CHAPTER II

Numerical Methods

II.1   The ACCRE Compute Cluster

II.1.1   Compute Nodes

II.1.1.1   x86_64 Nodes

II.1.1.2   GPU Nodes

II.1.2   Network

II.1.3   Filesystem

II.1.4   Scheduling

II.2   Initialization Code

II.2.1   Sampling the Power Spectrum

II.2.1.1   Cosmological Parameters

II.2.1.2   Sampling

II.2.2   Particle Displacement with ZA

II.2.3   Particle Displacement with 2LPT

II.3   GADGET2

II.3.1   Subsection1

II.3.1.1   Subsubsection1

II.3.1.2   Subsubsection2

II.3.2   Subsection2

II.4   ROCKSTAR

II.4.1   Subsection1

II.4.1.1   Subsubsection1

II.4.1.2   Subsubsection2

II.4.2   Subsection2

II.5   CROSSMATCH

II.5.1   Subsection1

II.5.1.1   Subsubsection1

CHAPTER III

Exploring Dark Matter Halo Populations in 2LPT and ZA Simulations

We study the structure and evolution of dark matter halos from $z = 300$ to $z = 6$ for two cosmological N-body simulation initialization techniques. While the second order Lagrangian perturbation theory (2LPT) and the Zel'dovich approximation (ZA) both produce accurate present day halo mass functions, earlier collapse of dense regions in 2LPT can result in larger mass halos at high redshift. We explore the differences in dark matter halo mass and concentration due to initialization method through three 2LPT and three ZA initialized cosmological simulations. We find that 2LPT induces more rapid halo growth, resulting in more massive halos compared to ZA. This effect is most pronounced for high mass halos and at high redshift, with a fit to the mean normalized difference between 2LPT and ZA halos as a function of redshift of $\mu_{\Delta M_{\mathrm{vir}}} = (7.88 \pm 0.17) \times 10^{-3} z - (3.07 \pm 0.14) \times 10^{-2}$. Halo concentration is, on average, largely similar between 2LPT and ZA, but retains differences when viewed as a function of halo mass. For both mass and concentration, the difference between typical individual halos can be very large, even for symmetrically distributed quantities, highlighting the shortcomings of ZA-initialized simulations for high-z halo population studies.

III.1 Introduction

The pre-reionization epoch is a time of significant evolution of early structure in the universe. Rare density peaks in the otherwise smooth dark matter (DM) sea lead to the collapse and formation of the first dark matter halos. The non-linear gravitational dynamics of halo formation lead to a diverse array of halo structure that continues to evolve internally and interact with the surrounding medium. This growth, whether due to mergers or accretion, plays a pivotal role in shaping a halo's properties.

These early-forming dark matter halos provide an incubator for the baryonic processes

that transform the surrounding space and allow galaxies to form. Initial gas accretion can lead to the formation of the first Pop-III stars (Couchman & Rees, 1986; Tegmark et al., 1997), which, upon their death, can collapse into the seeds for supermassive black holes (SMBHs) (Madau & Rees, 2001; Volonteri et al., 2003; Islam et al., 2003; Tanaka & Haiman, 2009; Alvarez et al., 2009; Jeon et al., 2012; Micic et al., 2011) or enrich the surrounding medium with metals through supernovae (Heger et al., 2003). Early supernovae enrich the surrounding medium with newly-formed metals as further star formation populates the first galaxies. The combined radiation from these early sources plays a key role in re-ionizing the universe by around $z = 6$. Additionally, halo mergers can drastically increase the temperature of halo gas through shock heating, increasing X-ray luminosity (Sinha & Holley-Bockelmann, 2009), and contribute to the unbinding of gas to form the warm-hot intergalactic medium (Sinha & Holley-Bockelmann, 2010).

While a number of parameters are required to fully characterize a DM halo, a first-order description can be obtained from it's mass and density profile. There are a number of ways to define a halo's mass. This becomes significant for mass-sensitive studies, such as the halo mass function (Press & Schechter, 1974; Reed et al., 2007; Heitmann et al., 2006; Lukić et al., 2007), the number density of halos as a function of mass and a key probe of cosmology. For a review, see, e.g., White (2001) and references therein. Additionally, see Voit (2005) and references therein for a more observation-focused discussion.

From a simulation standpoint, the two most common ways to obtain halo mass are to define either spherical overdensity halos or friends-of-friends (FOF) halos. The spherical overdensity method identifies regions above a certain density threshold, either with respect to the critical density $\rho_c = 3H^2/8\pi G$ or the background density $\rho_b = \Omega_m \rho_c$, where Ω_m is the matter density of the universe. The mass is then the mass enclosed in a sphere of some radius with mean density $\Delta \rho_c$, where Δ commonly ranges from ~ 100 to ~ 500. Alternatively, the FOF method finds particle neighbors and neighbors of neighbors defined to be within some separation distance (Einasto et al., 1984; Davis et al., 1985). Halo mass,

then, is simply the sum of the masses of the constituent particles.

Halo concentration $c \equiv R_{\mathrm{vir}}/r_s$ provides a useful measure of halo structure. Here, R_{vir} is the halo's virial radius, and r_s is the break radius between the inner $\sim r^{-1}$ and outer $\sim r^{-3}$ density profiles. A number of studies use cosmological simulations to explore concentration and its dependence on halo mass, environment, and cosmology (Navarro et al., 1997a; Bullock et al., 2001; Eke et al., 2001; Neto et al., 2007; Gao et al., 2008; Macciò et al., 2008; Muñoz-Cuartas et al., 2011; Klypin et al., 2011), merger and mass accretion histories (Wechsler et al., 2002; Zhao et al., 2003, 2009), and rms fluctuation amplitude of the linear density field $\sigma(M,z)$ (Prada et al., 2012).

Simulating early structure formation is difficult. The subtle $\mathcal{O}(10^{-5})$ density perturbations in place at the CMB epoch are vulnerable to numerical noise and intractable to simulate directly. Instead, a displacement field is applied to the particles to evolve them semi-analytically, nudging them from their initial positions to an approximation of where they should be at a more reasonable starting redshift for the numerical simulation. Starting at a later redshift saves computation time as well as avoiding the errors introduced by simulating noise.

The Zel'dovich approximation (Zel'dovich, 1970; Klypin & Shandarin, 1983; Efstathiou et al., 1985) and 2nd-order Lagrangian Perturbation Theory (Buchert, 1994; Buchert et al., 1994; Bouchet et al., 1995; Scoccimarro, 1998; Sirko, 2005; Crocce et al., 2006; Jenkins, 2010) are the two canonical frameworks for initial particle displacement. The Zel'dovich approximation (ZA, hereafter) is a linear displacement field, while 2nd-order Linear Perturbation Theory (2LPT, hereafter) adds a second-order correction term to the expansion.

Following Jenkins (2010), we briefly outline the second-order Lagrangian perturbation theory and compare it to the Zel'dovich approximation. In 2LPT, a displacement field $\Psi(q)$ is applied to the initial positions q to yield the Eulerian final comoving positions

$$x = q + \Psi. \tag{III.1}$$

The displacement field is given in terms of two potentials $\phi^{(1)}$ and $\phi^{(2)}$ by

$$x = q - D_1 \nabla_q \phi^{(1)} + D_2 \nabla_q \phi^{(2)} \qquad \text{(III.2)}$$

with linear growth factor D_1 and second-order growth factor $D_2 \approx -3D_1^2/7$. The subscripts q refer to partial derivatives with respect to the Lagrangian coordinates q. Likewise, the comoving velocities are given, to second order, by

$$v = -D_1 f_1 H \nabla_q \phi^{(1)} + D_2 f_2 H \nabla_q \phi^{(2)} \qquad \text{(III.3)}$$

with Hubble constant H and $f_i = \mathrm{d}\ln D_i / \mathrm{d}\ln a$, with expansion factor a. The relations $f_1 \approx \Omega^{5/9}$ and $f_2 \approx 2\Omega^{6/11}$, with matter density Ω, apply for flat models with a non-zero cosmological constant (Bouchet et al., 1995). The f_1, f_2, and D_2 approximations here are very accurate for most actual ΛCDM initial conditions, as Ω is close to unity at these high redshifts. We may derive $\phi^{(1)}$ and $\phi^{(2)}$ by solving a pair of Poisson equations

$$\nabla_q^{(1)}(q) = \delta^{(1)}(q) \qquad \text{(III.4)}$$

with linear overdensity $\delta^{(1)}(q)$, and

$$\nabla_q^{(2)}(q) = \delta^{(2)}(q). \qquad \text{(III.5)}$$

The second order overdensity $\delta^{(2)}(q)$ is related to the linear overdensity field by

$$\delta^{(2)}(q) = \sum_{i>j} \left\{ \phi_{,ii}^{(1)}(q)\phi_{,jj}^{(1)}(q) - \left[\phi_{,ij}^{(1)}(q) \right]^2 \right\} \qquad \text{(III.6)}$$

where $\phi_{,ij} \equiv \partial^2 \phi / \partial q_i \partial q_j$. For initial conditions from the Zel'dovich approximation, or first-order Lagrangian initial conditions, the $\phi^{(2)}$ terms of equations (III.2) and (III.3) are ignored.

Cosmological simulations that follow the initial collapse of dark matter density peaks into virialized halos often neglect to consider the nuances of initialization method. Non-linear decaying modes, or transients, will be damped as $1/a$ in ZA. In 2LPT, however, transients are damped more quickly as $1/a^2$. It should be expected, then, that structure in 2LPT will be accurate after few e-folding times than in ZA (Scoccimarro, 1998; Crocce et al., 2006; Jenkins, 2010). The practical result is that high-σ DM density peaks at high redshift are suppressed in ZA compared with 2LPT for a given starting redshift.

One facet often overlooked is appropriate starting redshift determined by box size and resolution (Lukić et al., 2007). Initialization with 2LPT allows for a later starting redshift compared with an equivalent ZA-initialized simulation. However, many ZA simulations do not take this into account, starting from too late of an initial redshift (Crocce et al., 2006; Jenkins, 2010). In order to characterize an appropriate starting redshift, the relation between the initial rms particle displacement and mean particle separation must be considered. The initial rms displacement Δ_{rms} is given by

$$\Delta_{\mathrm{rms}}^2 = \frac{4\pi}{3} \int_{k_f}^{k_{\mathrm{Ny}}} P(k, z_{\mathrm{start}}) \mathrm{d}k, \tag{III.7}$$

where $k_f = 2\pi/L_{\mathrm{box}}$ is the fundamental mode, L_{box} is the simulation box size, $k_{\mathrm{Ny}} = \frac{1}{2}Nk_f$ is the Nyquist frequency of an N^3 simulation, and $P(k, z_{\mathrm{start}})$ is the power spectrum at starting redshift z_{start}. In order to avoid the "orbit crossings" that reduce the accuracy of the initial conditions, Δ_{rms} must be some factor smaller than the mean particle separation $\Delta_p = L_{\mathrm{box}}/N$ (Holley-Bockelmann et al., 2012). For example, making orbit crossing a $\sim 10\sigma$ event imposes $\Delta_{\mathrm{rms}}/\Delta_p = 0.1$. However, for small-volume, high-resolution simulations, this quickly leads to impractical starting redshifts. Continuing our example, satisfying $\Delta_{\mathrm{rms}}/\Delta_p \sim 0.1$ for a $10h^{-1}$ Mpc, 512^3 simulation suggests $z_{\mathrm{start}} \approx 799$. Starting at such a high redshift places such a simulation well into the regime of introducing errors from numerical noise caused by roundoff errors dominating the smooth potential. A more

relaxed requirement of $\Delta_{\mathrm{rms}}/\Delta_p = 0.25$ yields $z_{\mathrm{start}} = 300$, which we adopt for this work.

While differences in ensemble halo properties, such as the halo mass function, between simulation initialization methods are mostly washed away by $z = 0$ (Scoccimarro, 1998), trends at earlier redshifts are less studied (Lukić et al., 2007). In this paper, we explore the effects of ZA and 2LPT on the evolution of halo populations at high redshift. It is thought that 2LPT allows initial DM overdensities to get a "head start" compared with ZA, allowing earlier structure formation, more rapid evolution, and larger possible high-mass halos for a given redshift. We explore this possibility by comparing halo properties in (otherwise identical) simulations initialized with ZA and 2LPT.

We discuss the simulations, halo finding, and analysis methods in Section III.2, results in Section III.3, implications, caveats, and future work in Section III.4, and finally summarize our results and conclude in Section IV.4.

III.2 Numercial Methods

We use the Nbody tree/SPH code GADGET-2 (Springel et al., 2001; Springel, 2005) to evolve six dark matter–only cosmological volumes from $z_{start} = 300$ to $z = 6$ in a ΛCDM universe. Each simulation is initialized using WMAP-5 parameters. For each of the three simulation pairs, we directly compare 2LPT and ZA by identically sampling the CMB transfer function and displacing the initial particle positions to the same starting redshift using 2LPT and ZA. The three sets of simulations differ only by the initial phase sampling random seed. Each volume contains 512^3 particles in a 10 h^{-1} Mpc box. Full simulation details are discussed in Holley-Bockelmann et al. (2012).

For each of our six simulations, we use the 6-D phase space halo finder code ROCKSTAR (Behroozi et al., 2013) to identify spherical overdensity halos at each timestep. ROCKSTAR follows an adaptive hierarchical refinement of friends-of-friends halos in 6-D phase space, allowing determination of halo properties such as halo mass, position, virial radius, internal energy, and number of subhalos. ROCKSTAR tracks halos down to a threshold of around 20

11

particles, but we use a more conservative 100 particle threshold for our analysis. We use all particles found within the virial radius to define our halos and their properties.

We match halos between companion simulations by comparing constituent particle IDs. We identify matching halos based on the highest fraction of matching particles contained in each at any given timestep. We remove subhalo matches (i.e. a halo must not be contained within another halo) and halo pairs with fewer than 100 particles in either 2LPT or ZA. We are left with approximately 60,000 total halo pairs for our three boxes at $z = 6$. With halo catalogues matched between simulations, we can compare properties of individual corresponding halos. We "stack" the three simulation boxes for each initialization method, and combine the halos from each into one larger sample in our analysis.

Halo concentration $c = R_{vir}/R_s$ is derived from ROCKSTAR's output for R_s and R_{vir}, where R_s is the scale radius defined by the NFW (Navarro et al., 1996) profile

$$\rho(r) = \frac{\rho_0}{\frac{r}{R_s}\left(1 + \frac{r}{R_s}\right)^2} \tag{III.8}$$

and R_{vir} is the virial radius as defined by Bryan & Norman (1998). To verify the accuracy of the ROCKSTAR fit, we independently find density profiles for several halos and compare the fit parameters such as R_s. For each halo, we fit an NFW density profile to logarithmic radial bins of particle position with a non-linear least squares fitting routine from the SciPy library. From this, we measure the scale radius and, along with virial radii from ROCKSTAR, the concentration. The bottom two rows of Figure III.1, for example, show the fitting results for a particle matched halo pair. For halos fit by our method, our results are in relatively good agreement with ROCKSTAR. However, as we do not find an acceptable fit for every halo, we use the more complete ROCKSTAR data for the final concentration measurements. However, we do note that ROCKSTAR does not provide goodness-of-fit parameters for it's internal density profile measurements used to derive concentration, so error estimates for concentration values of individual halos are unknown. Additionally, proper density profile

fitting is non-trivial, as the non-linear interactions of numerical simulations rarely result in simple spherical halos that can be well described using spherical bins.

Figure III.1 also makes evident the difficulty in fitting density profiles and obtaining concentration measurements for typical realistic halos. Large substructure, as displayed by the ZA halo, can defeat the radial symmetry of the halo and cause significant deviations in the density profile. Centering can also be an issue in these cases. Due to these complications, there are a number of approaches for finding halo concentrations (Prada et al., 2012), but for consistency, we use the values derived from ROCKSTAR's fitting for our concentration measurements.

III.3 Results

With our catalog of matched dark matter halos, we are able to directly compare differences in halo properties arising from initialization with 2LPT vs ZA. We consider halos on a pair–by–pair basis as well as the entire sample as a whole. Overall, we find 2LPT halos to have undergone more growth at a given redshift than their ZA counterparts.

III.3.1 Individual halo pairs

We compare morphologies, density profiles, and various other halo properties for halo pairs on an individual halo–by–halo basis by eye for several of the most massive halos. Morphologies appear fairly similar for most halos, indicating good halo matches between simulations. However, some pairs display a differences in central morphology, in which one halo will have more than one density peak, or in the case of both halos having multiple density peaks, one halo having a larger separation between peaks than the other. We interpret these cases to be examples of differences in merger epochs, in which case one halo may still be undergoing a major merger, while it's companion is in a more relaxed post-merger state. We give an example of one such pair at $z = 6$ in Figure III.1. The top two rows show density projections of the central nuclear region for a large 2LPT and matching ZA halo (first and second rows, respectively). We find the ZA halo to contain two distinct density

peaks with a separation of ~ 10 kpc, while the 2LPT halo displays only a single core. On the third and fourth rows, we plot the density profiles of the same two halos (2LPT and ZA, respectively). Here, with nearly identical virial radii, it is readily seen that the smaller R_{s} for the 2LPT halo produces a larger concentration value than is derived for the ZA halo.

III.3.2 Difference distributions of halo properties

Expanding to an analysis of the halo population as a whole, we consider distributions of halo virial mass M_{vir}, concentration c, central density offset X_{off}, defined as the distance between the halo density peak and the halo center of mass (Behroozi et al., 2013), and a number of other halo parameters. For each quantity q, we create histograms of Δq, the normalized difference in q between halos in the 2LPT and ZA simulations

$$\Delta q = \frac{q_{\text{2LPT}} - q_{\text{ZA}}}{q_{\text{avg}}} \tag{III.9}$$

for each simulation snapshot. Of these, distributions for ΔM_{vir} and Δc are the most interesting, with the remainder mostly conforming to the pattern of Gaussians centered about $\Delta q = 0$.

We briefly note, however, that the symmetry of distributions for relaxation-tracking parameters like ΔX_{off} might be unexpected at first glance. As noted above, 2LPT halos should have more rapid evolution and potentially earlier mergers than their ZA counterparts, suggesting that we would preferentially find them in a more relaxed state. However, the lack of average difference between 2LPT and ZA indicates that the picture is not as simple as this. Nuclear displacement may be caught, for example, at a larger value after periapsis passage, while a less-evolved merger may be caught closer to periapsis and thus appear with smaller X_{off}.

We plot histograms of ΔM_{vir} and Δc in the left and right columns, respectively, of Figure III.2 for three representative timesteps at redshifts of $z = 14.7$, $z = 10.3$, and $z = 6.0$. For each panel, the blue histogram includes the entire included halo sample, and the smaller

gray-filled green histogram includes only the top 25% most massive halos. Fits to the primary histograms are overplotted as red dashed curves.

We note that much of our data appears centrally peaked and not well described by a standard Gaussian distribution. Therefore, for each distribution, in order to additionally account for excess kurtosis, we fit a generalized normal distribution (Nadarajah, 2005) with probability density function

$$f(x) = \frac{\beta}{2\alpha\Gamma(1/\beta)} e^{(|x-\mu|/\alpha)^{\beta}}, \tag{III.10}$$

where μ is the mean, α is the scale parameter, β is the shape parameter, and Γ is the gamma function

$$\Gamma(t) = \int_0^{\infty} x^{t-1} e^{-x} dx. \tag{III.11}$$

The shape parameter β is restricted to $\beta \geq 1$. This allows the distribution to potentially vary from a Laplace distribution ($\beta = 1$) to a uniform distribution ($\beta = \infty$) and includes the normal distribution ($\beta = 2$). The distribution has variance

$$\sigma^2 = \frac{\alpha^2 \Gamma(3/\beta)}{\Gamma(1/\beta)} \tag{III.12}$$

and excess kurtosis

$$\gamma_2 = \frac{\Gamma(5/\beta)\Gamma(1/\beta)}{\Gamma(3/\beta)^2} - 3. \tag{III.13}$$

The distribution is symmetric, and thus has no skewness by definition. As such, the values for skew presented below are measured directly from the data and do not rely on the fit to the histograms.

From a high redshift, we find a tendency for 2LPT halos to be more massive. The mean is consistently positive (heavier 2LPT halos) and is most displaced from zero at high redshift. The peak of the distribution gradually moves closer to zero as we progress in redshift. We find the least difference between paired halos for the final snapshot at $z = 6$.

15

These trends with redshift are discussed in more detail below.

The higher-order moments of the ΔM_{vir} distribution are of interest as well, as we find significant deviation from the standard Gaussian distribution that one might expect. We find the distribution to be much closer to a Laplace distribution, with shape parameter consistently sitting at or very close to $\beta = 1$. When compared to a Gaussian distribution, the larger excess kurtosis implies a sharper central peak and heavier outlier tails. We note that, as we have required $\beta \geq 1$ when fitting the data in order to not allow the fitting distribution to be more peaked than the Laplace distribution, the kurtosis of the data itself could potentially be even higher than what is represented by the fit.

As we use the symmetrical generalized normal distribution as our fit function, the skewness of the data is unable to be measured from the fit itself. However, a qualitative deviation from symmetry can be readily observed. By $z = 6$, we end up with a rather symmetrical distribution, with both sides of the histogram equally well described by our fit. However, at higher redshift, we note a marked increase in skewness and deviation from this symmetry. As redshift increases, we observe an increasing difference between the fit curve and the bins to the left of the histogram peak.

We find no no overall preference for more concentrated 2LPT or ZA halos. In contrast to the ΔM_{vir} histograms , Δc shows very little deviation from symmetry about zero. Throughout the simulation, we find the distributions to have a mean close to zero and negligible skew. The widths of the distributions are much wider than those for ΔM_{vir}. As with mass, concentration histograms are sharply peaked with heavy tails.

III.3.3   Trends with redshift

In Figure III.3, we more quantitatively assess the time progression of our various trends hinted at in Figure III.2. Here, we plot the mean, root mean square (RMS), standard deviation, skew, and kurtosis for ΔM_{vir} and Δc as functions of redshift. Uncertainty in the mean is estimated directly by the least squares fitting routine.

As our fitting distributions are symmetrical and skew must therefore be measured directly from the data, in order to derive uncertainties for skew, we measure the skew of the distributions for each of our three simulation boxes individually as well as for the single stacked data set. Uncertainty in skew is then simply the standard deviation of the mean of the skew of the three individual boxes.

Determining the uncertainty in the kurtosis is slightly more involved, as kurtosis is determined by a transformation of the generalized normal distribution's shape parameter β according to (III.13). Following the standard procedure for propagation of uncertainty, we calculate the standard deviation of the kurtosis as

$$s_{\gamma_2} = \sqrt{\left(\frac{d\gamma_2}{d\beta}\right)^2 s_\beta^2} \tag{III.14}$$

$$= s_\beta \frac{d}{d\beta}\left[\frac{\Gamma(5/\beta)\Gamma(1/\beta)}{\Gamma(3/\beta)^2} - 3\right]. \tag{III.15}$$

The derivative of the gamma function is

$$\Gamma'(x) = \Gamma(x)\psi_0(x) \tag{III.16}$$

where the digamma function ψ_0 is the derivative of the logarithm of the gamma function and is given by

$$\psi_0(x) = \int_0^\infty \left(\frac{e^{-t}}{t} - \frac{e^{-xt}}{1 - e^{-t}}\right) dt \tag{III.17}$$

if the real part of x is positive. Now, taking the derivative of γ_2 and doing a bit of algebra gives us

$$s_{\gamma_2} = s_\beta \frac{1}{\beta^2}(\gamma_2 + 3)\left[6\psi_0(3/\beta) - 5\psi_0(5/\beta) - \psi_0(1/\beta)\right], \tag{III.18}$$

with which we can find the uncertainty in the kurtosis given the value and uncertainty of the shape parameter β estimated from the least squares fit routine.

The mean for ΔM_{vir} is positive and highest at high redshift, trending toward zero by the

Table III.1: Coefficients for linear least squares fits from Figure III.3.

	ΔM_{vir}	Δc
A	$(7.88 \pm 0.17) \times 10^{-3}$	$(3.62 \pm 0.95) \times 10^{-3}$
B	$(-3.07 \pm 0.14) \times 10^{-2}$	$(-2.34 \pm 0.84) \times 10^{-2}$

end of the simulation. Distributions for Δc retain means close to and consistent with zero. Standard deviation decreases slightly for both ΔM_{vir} and Δc.

We find least square linear fits for both mean ΔM_{vir} vs z and mean Δc vs z. Coefficients for slope A and y-intercept B for the fit equation $\mu = Az + B$ are given in Table III.1 for both cases. (Note the reversed redshift axes for the sign of the slopes.) We find a significant trend for ΔM_{vir}, with a slope $\sim 46\sigma$ from zero. Conversely, the slope for Δc is much smaller and, considering the larger spread of the underlying distributions, can be considered negligible. For ΔM_{vir}, the y-intercept coefficient B likely has little meaning in terms of the actual behaviour at $z = 0$, as we expect the trend to level out at later redshift.

We do note, however, that the mean can be deceiving as an indicator of total difference between halo populations, especially when it is close to zero as with concentration. It should be noted that while the mean can indicate a lack of average difference between the whole sample of 2LPT and ZA halos, there can still be very large discrepancies between many individually paired halos. We visualize this by plotting the RMS of ΔM_{vir} and Δc, which is plotted as a green dotted line. Unlike the mean, standard deviation,and kurtosis, which are measured from fits to the histograms, RMS is measured directly from the data and is not dependent on fitting. The large RMS values are indicative of how much overall difference can arise between 2LPT and ZA halos, even though the differences may average to zero when considering the entire population. The RMS for both ΔM_{vir} and Δc starts highest at high redshift and steadily decreases throughout the simulation, reaching a minimum by $z = 6$.

Additionally, it is of interest to consider the percentage of halo pairs that are "wrong" at some given time, regardless of whether the quantity is higher in 2LPT or ZA. For example,

if we count halos outside a slit of width $\varepsilon = \pm 10\%$ around $\Delta q = 0$, we find that by $z = 6$, 14.6% of halo pairs still have substantially mismatched masses. Likewise, 74.3% have mismatched concentrations. It is evident that many halo pairs can have markedly different growth histories, even when the ensemble halo populations have similar distributions.

Kurtosis is consistently large (more peaked than a Gaussian distribution) for both mass and concentration, with a slight increasing trend throughout the simulation for concentration. Skew is positive for much of the simulation for mass, but is much smaller for concentration. These higher moment deviations from Gaussianity hint at the non-linear dynamics at play in halo formation.

The large excess kurtosis indicates a sharper peak and heavier tails than a Gaussian for the underlying distribution. This may indicate a fair amount of sensitivity to initial differences in halo properties, in that halo pairs that start out within a certain range of the mean are more likely move closer to the mean, while pairs that are initially discrepant will diverge even further in their characteristics. This is further supported by a kurtosis that increases with time.

The skew at high redshift for ΔM_{vir} may give another hint at the non-linear halo formation process. Runaway halo growth causes more massive halos to favor faster mass accretion and growth. The positively skewed distributions show a picture of 2LPT halo growth in which initial differences in mass are amplified the most readily in the earliest forming and most massive halos, again indicating the extra kick-start to halo growth provided by 2LPT initialization. While the slight decrease in skew with redshift may be counter-intuitive to this notion, it is likely that rising noise floor of the large amounts of newly formed halos begin to mask the signal from the smaller number of large halos displaying this effect.

III.3.4   Trends with halo mass

We consider ΔM_{vir} and Δc as a function of average halo mass $M_{\mathrm{vir,avg}} = (M_{\mathrm{vir,2LPT}} + M_{\mathrm{vir,ZA}})/2$ in Figure III.4. The data is binned on a 2-D grid with a logarithmic color map

for three representative timesteps. A linear fit to the data is overplotted in red, and a dotted blue line is provided at $\Delta M_{vir} = 0$ and $\Delta c = 0$ to guide the eye.

We find that ΔM_{vir} tends to increase with increasing $M_{\mathrm{vir,avg}}$, a trend that is, again, most pronounced at high redshift. 2LPT halos are consistently more massive than their ZA counterparts, with the difference increasing with average halo mass. While less massive halo pairs have a larger spread in the difference in 2LPT and ZA mass, more massive halo pairs are more consistently heavier in 2LPT than in ZA. The slope of the fit line trends towards zero as we progress in redshift, with little average mass dependence by $z = 6$.

We find a small trend for more massive halo pairs to be more concentrated in ZA, but this trend is weaker than for ΔM_{vir}. This negative slope can be expected, as halo concentartion is expected to decrease with increasing mass (Bullock et al., 2001), and we find high mass halos to be more massive in 2LPT than in ZA. The data have a larger variance than ΔM_{vir}, and fits have and overall shallower slope. Mass dependence all but disappears by $z = 6$. To reconcile these trends with the symmetrical concentration distributions of Figure III.2, we note that the trends in mass may be hidden by integration across the entire mass range and still result in overall Δc distributions symmetric about zero.

III.4 Discussion

As we evolve our DM halo population from our initial redshift to $z = 6$, we find that simulation initialization with 2LPT can have a significant effect on halo population compared to initialization with ZA. The second order displacement boost of 2LPT provides a head start on the initial collapse and formation of DM halos. This head start manifests itself further along in a halo's evolution as more rapid growth and potentially earlier mergers. 2LPT halos are, on average, more massive than their ZA counterparts. The larger mass for 2LPT halos is more pronounced for higher mass pairs, while 2LPT halo concentration is larger on the small mass end. Both mass and concentration differences trend towards symmetry about zero as halos evolve in time, with the smallest difference observed at the end of the

simulations at $z = 6$. Casual extrapolation of our observed trends with redshift to today would indicate that 2LPT and ZA would produce very similar halo populations by $z = 0$. However, the larger differences at high redshift should not be ignored.

The earlier formation times and larger masses of halos seen in 2LPT-initialized simulations could have significant implications with respect to early halo life during the Dark Ages. Earlier forming, larger halos affect the formation of Pop-III stars, and cause SMBHs to grow more rapidly during their infancy (Holley-Bockelmann et al., 2012). The epoch of peak star formation may also be shifted earlier. This could additionally affect the contribution of SMBHs and early star populations to re-ionization. Larger halos may also influence studies of the high-z halo mass function, abundance matching, gas dynamics, AGN, clustering, and large scale structure formation.

In these discussions, it is important to note that it is wrong to assume that the ZA halo properties are the "correct" halo properties, even in a statistical sense. While halo mass suggests the most obvious shortcoming of ZA simulations, even properties such as concentration that show little difference on average between 2LPT and ZA can have large discrepancies on an individual halo basis. Failure to consider uncertainties in halo properties for high z halos in ZA simulations can lead to catastrophic errors.

We note a few caveats with our simulations and analysis. We did not exclude substructure when determining the properties of a halo, so care must be taken when comparing to works which remove subhalo particles in determining halo mass and concentration. Halo matching is not perfect, as it is based on one snapshot at a time, and may miss count halos due to merger activity and differences in merger epochs. However, we believe this effect to be minor. While we compared ROCKSTAR's output with our own fitting routines and found them to be in good agreement, ROCKSTAR does not provide goodness of fit parameters for its NFW profile fitting and R_s measurements. It also may be debated whether it makes sense to even consider concentration of halos at high redshift which are not necessarily fully virialized.

We use a simulation box size of only 10 Mpc. This is too small to effectively capture very large outlier density peaks. We would, however, expect these large uncaptured peaks to most affected by 2LPT initialization, so the effects presented here may even be dramatically underestimated. Additionally, a larger particle number would allow us to consider smaller mass halos than we were able to here, and to better resolve all existing structure. A higher starting redshift could probe the regime where 2LPT initialization contributes the most. It would also be of interest to evolve our halo population all the way to $z = 0$. The addition of baryons in a fully hydrodynamical simulation could also affect halo properties. These points may be address in future studies.

III.5 Conclusion

We analyzed three 2LPT and ZA simulation pairs and tracked the spherical overdensity dark matter halos therein with the 6-D phase space halo finder code ROCKSTAR to compare the effect of initialization technique on properties of particle–matched dark matter halos. This approach allowed us to directly compare matching halos between simulations and isolate the effect of using 2LPT over ZA. In summary, we found the following:

- 2LPT halos get a head start in the formation process and grow faster than their ZA counterparts.

- 2LPT halos are, on average, more massive than ZA halos. Earlier collapse of the largest initial density peaks causes this effect to be most pronounced for the most massive halos.

- Halo concentration, on average, is similar for 2LPT and ZA halos. However, halo pairs shift to more concentrated 2LPT halos in the low mass regime and more concentrated ZA halos in the high mass regime.

- Little difference, on average, is found between the average nuclear displacement of 2LPT and ZA halos.

22

- Differences in halo properties such as mass and concentration between 2LPT and ZA halos are most pronounced for high redshift. The distributions begin to settle toward symmetry by the end of the simulations.
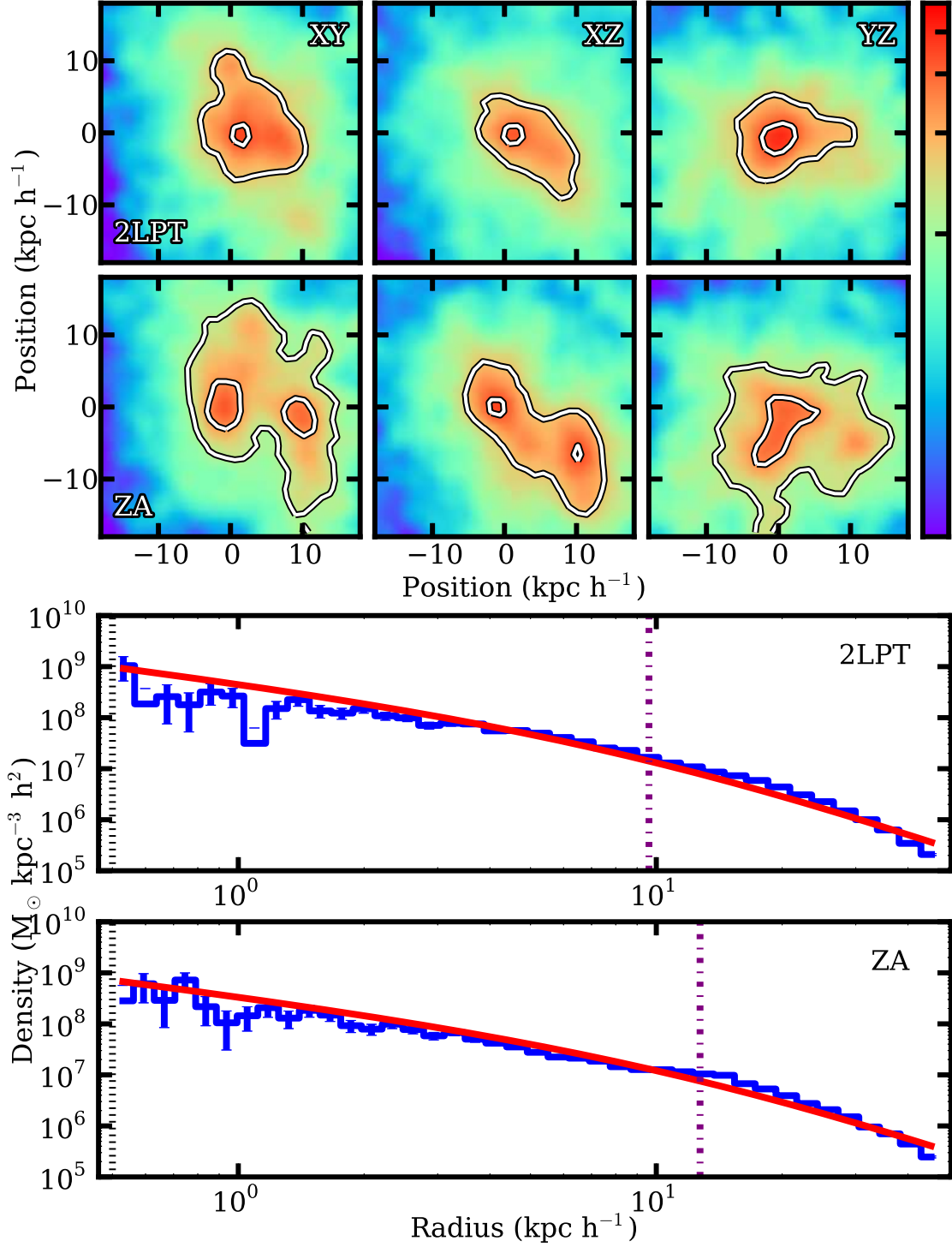
Figure III.1: *Top two rows:* Density projections for two matching halos at $z = 6$. The first and second row are 2LPT and ZA, respectively. The halos appear to be either undergoing or have recently undergone a major merger. The 2LPT halo appears to be more relaxed and further along in the merger process, while the ZA halo lags behind, still displaying two distinct cores. *Bottom two rows:* Density profiles for the same two halos as above. NFW profiles are fit to logarithmic radial bins of particle position and are overplotted as red curves. The purple dot–dash lines mark the scale radii. The black dotted lines mark the resolution limit of the simulations.
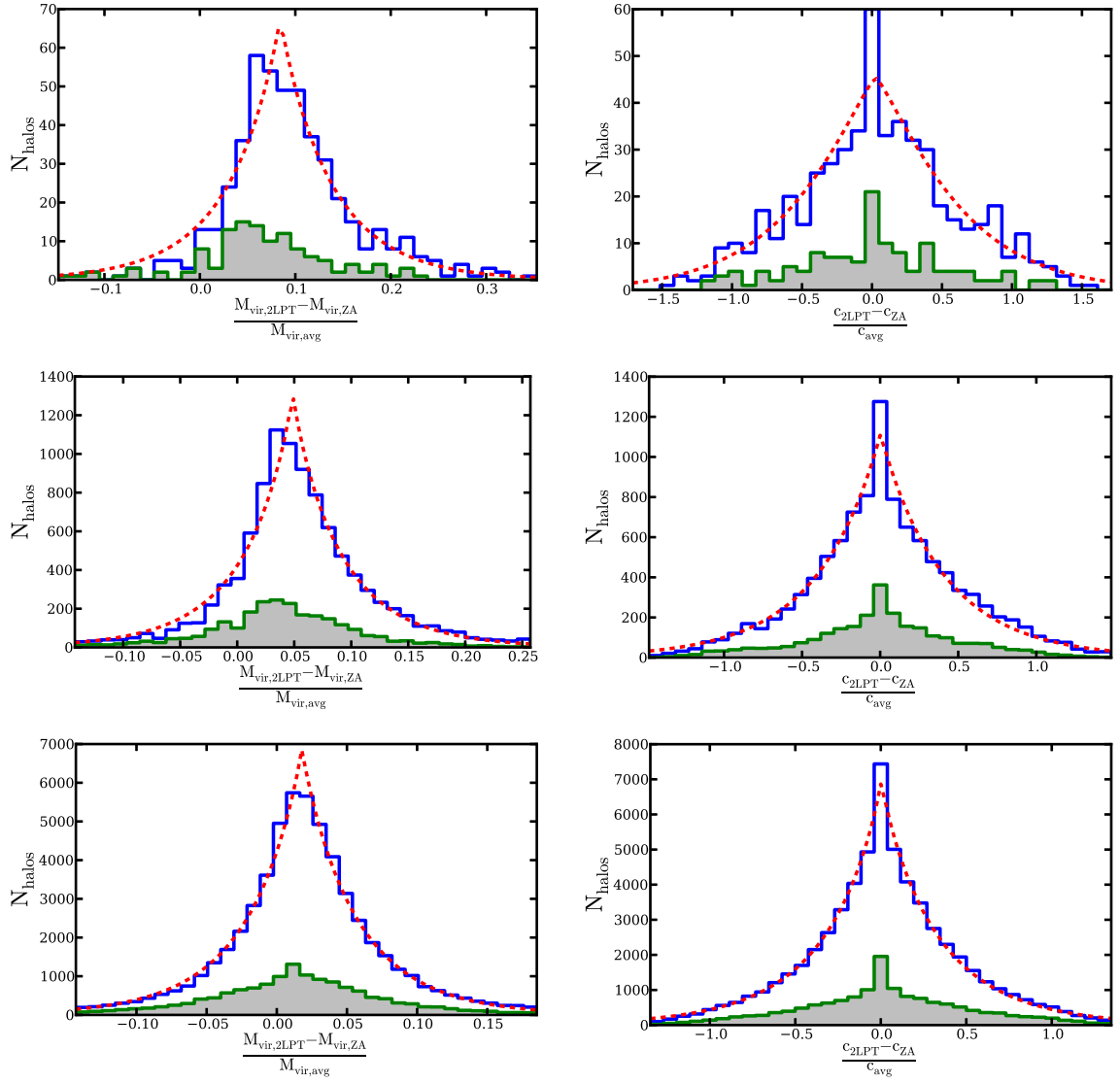
Figure III.2: Histograms of $\Delta M_{\rm vir}$ (*left column*) and Δc (*right column*) for snapshots at $z = 14.7$, $z = 10.3$, and $z = 6.0$ (*top, middle, and bottom panels, respectively*). The small gray-filled histograms count only the top 25% most massive halos. The main histograms are fit with a generalized normal distribution with parameters for mean, scale, and shape, overplotted as the red dashed line. The shape parameter allows a variable excess kurtosis and the additional inclusion of distribution shapes other than Gaussian. The distribution for $\Delta M_{\rm vir}$ has a positive mean and heavier 2LPT halos, with the most pronounced difference at high redshift. The skew of the distribution is also the most positive at high redshift, and shifts toward symmetry by $z = 6$. The Δc distribution remains symmetric about zero, with a mean of zero and negligible skew. Both distributions have excess kurtosis consistently larger than that of a standard Gaussian distribution, with a sharp peak and heavy tails.
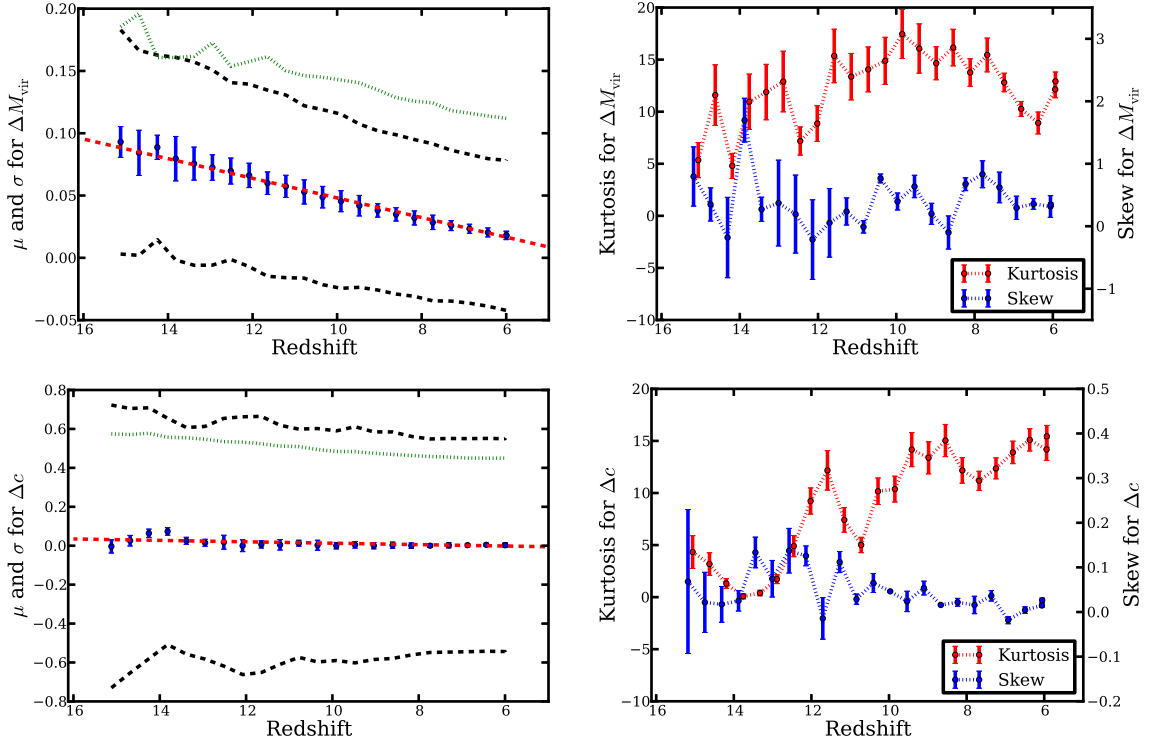
Figure III.3: Mean, standard deviation, and RMS (*left column*) and skew and excess kurtosis (*right column*) as functions of redshift for ΔM_{vir} (*top row*) and Δc (*bottom row*). In the left column, μ is plotted as blue points, and $\mu \pm \sigma$ is plotted as the black dashed line, and RMS values are plotted as a green dotted line. The red dashed line is a linear fit to the mean. We find a significant trend for μ for ΔM_{vir} to be more positive at higher redshift and gradually shift toward zero as the simulation progresses. The mean for Δc, however, remains at or very near zero for most of the simulation. The ΔM_{vir} and Δc distributions narrow over time, with a slight decrease in σ. In the right column, we plot skew (blue line) and excess kurtosis (red line). Skew is positive for much of the simulation for ΔM_{vir}, but is much smaller for Δc. Kurtosis is large (much more peaked than Gaussian) for both ΔM_{vir} and Δc throughout much of the simulation, and especially at later redshift.
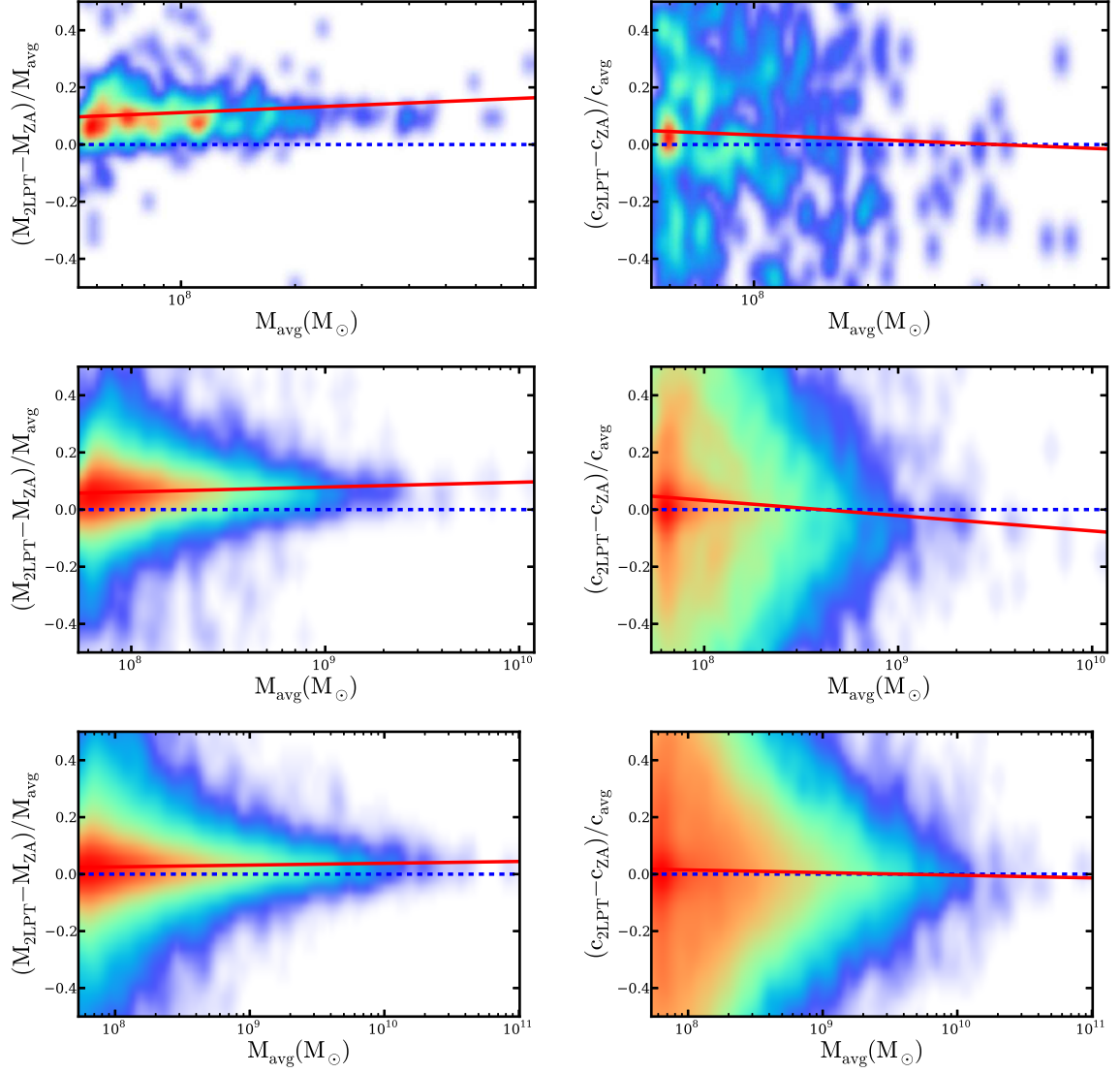
Figure III.4: ΔM_{vir} (left column) and Δc (right column) as functions of $M_{\text{vir,avg}}$. Halos are counted in 2-D rectangular bins and smoothed with a Gaussian kernel with a logarithmic color scale. The red line is the least-squares best fit to the data. The blue dashed line at zero is provided to guide the eye. The three rows again correspond to snapshots at $z = 14.7$, $z = 10.3$, and $z = 6.0$, respectively.

CHAPTER IV

Supermassive Black Holes and Their Hosts

IV.1 Introduction

The study of the evolution of galaxies and the growth of the supermassive black holes at their cores go hand in hand. Although the typical length scales for the two can vary by many orders of magnitude, they seem inexorably linked. Observational correlations between galaxy and supermassive black hole properties hint at an underlying co-evolution driven by shared mechanisms.

IV.1.1 Galaxy Properties

How do we describe a galaxy? Being extended, resolvable objects, galaxies provide a unique wealth of observable characteristics not obtainable from point sources such as stars. While many characteristics can be deduced about point sources, the actual observations themselves come down to measuring position on the sky and measuring flux as a function of frequency and time. From this information, all that we know about stars and other point sources, such as temperature, age, size, and composition, can be inferred. However, for extended objects like galaxies, we are given more to work with.

IV.1.1.1 Color

A galaxy's color is determined by its stellar component. While a galaxy in itself may be resolvable, for all but the most nearby of galaxies, individual stars are not. What we see when looking at a particular small section of a galaxy is the averaged-together light from stars in that section.

Broadly, bluer late-type spirals have a $u - r$ color of around $1.3 - 2.0$, while redder early-type galaxies have a $u - r$ color of around $2.3 - 2.7$. The color of a galaxy can be a good indicator for its age and evolutionary stage. Star formation processes generally tend

28

to produce many smaller, cooler, redder stars and fewer larger, hotter, bluer stars. These small, cool stars are much longer-lived than their massive counterparts, while the large, warm stars are much brighter. After star formation turns off, the short-lived blue stars begin to die off, and the galaxy becomes redder, as more of the fraction of total light comes from the red end of the population.

IV.1.1.2 Morphology

The extended nature of galaxies allows us to observe their morphology. The classification scheme originally devised by Hubble (1926) places galaxies into the four broad categories: elliptical, spiral, lenticular, and irregular. Elliptical galaxies tend to be larger, redder, have less gas, and dominated by more radial orbits. Spiral galaxies tend to be smaller, bluer, have more gas, and have more of a disk component. Spirals can have a number or arms, a central bulge, and a central bar. Lenticular galaxies are middle-of-the-road galaxies, with both a strong central bulge like an elliptical, and an extended disk like a spiral, however without spiral arms. Irregular galaxies tend to defy this simple classification scheme, and can be found in any number of configurations.

Figure IV.1 is a cartoon of the classification scheme. To the left of the diagram are elliptical galaxies. The subcategories are an indication of the shape of the galaxy, with the most spherical on the left and progressing to more flattened shapes to the right. On the right of the diagram are spiral galaxies. These are broken into two branches, based on whether or not the galaxy contains a central bar. Moving from right to left, the spiral arms of the galaxies become more tightly wound, and the central bulges become more dominant. At the center of the diagram where the spiral fork meets the elliptical line, lie lenticular galaxies. Irregular galaxies are, as the name would imply, irregular and do not fall on the diagram.
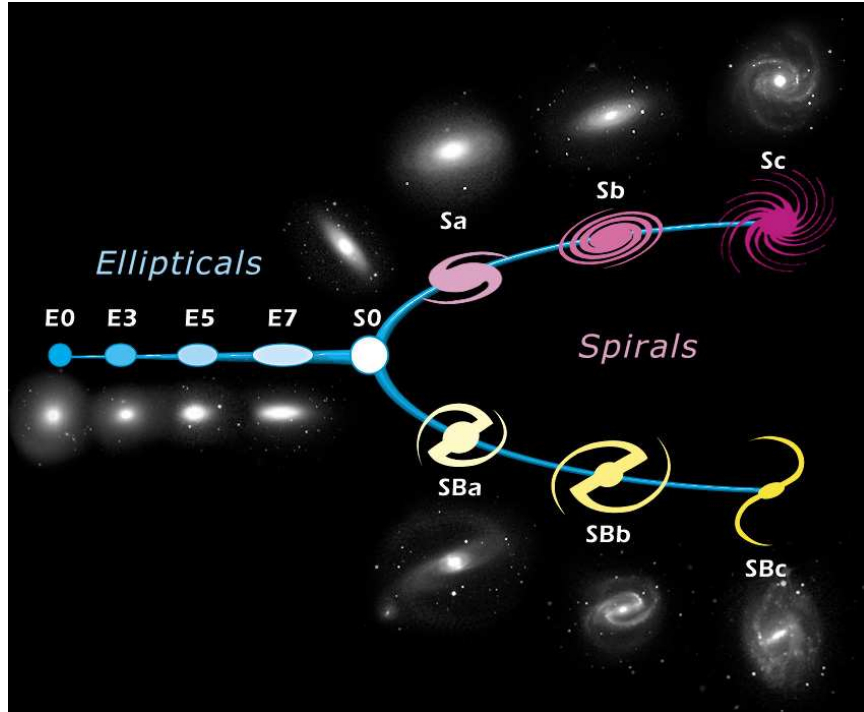
Figure IV.1: The Hubble tuning fork. On the left of the diagram are elliptical galaxies. E0 galaxies are the most spherical, while E7 are the most flattened or elongated. S0 are lenticular galaxies. The top branch on the right are spiral galaxies with no bar, while the bottom right branch are spiral galaxies with a bar. Both progress from tightly wound spiral arms and large bulges to loosely wound spiral arms and small to no bulges, going from Sa to Sc or SBa to SBc.

IV.1.2   Supermassive Black Hole Properties

A non-merging black hole, much like an elementary particle, can be described simply by its mass, charge, and spin. Its effect on its local spacetime, infalling matter, and surrounding environment all come back to these three parameters. However, determination of these parameters and the study of how black holes interact with their surroundings can be quite involved.

Black holes are, by their very nature, black, and difficult to observe. We cannot see light emitted directly from a black hole as we would a star, since a black hole is defined as an object massive and compact enough to not allow light within its event horizon to escape. We are forced, therefore, to employ other methods of measuring black holes.

Thus far, the majority of progress in the measurement of black hole properties has been in measuring mass. There are a number of ways to measure the mass of a black hole. Here, we will briefly discuss masers, stellar dynamics, gas dynamics, and reverberation mapping as methods of measuring a supermassive black hole's mass.

Astrophysical masers are sources of stimulated spectral line emission in the microwave band formed in regions of high-density gas comprised of molecules such as hydroxyl, formaldehyde, and water (Lo, 2005). Since the emission frequencies of these sources are very well constrained, high-accuracy Doppler shifts can be determined. These Doppler shifts can then be used to determine velocities for the masers, and thus how much mass is enclosed by their orbits. If these masers lie very close to the supermassive black hole (SMBH) in the center of their galaxy, the enclosed mass can be constrained to be primarily that of the SMBH.
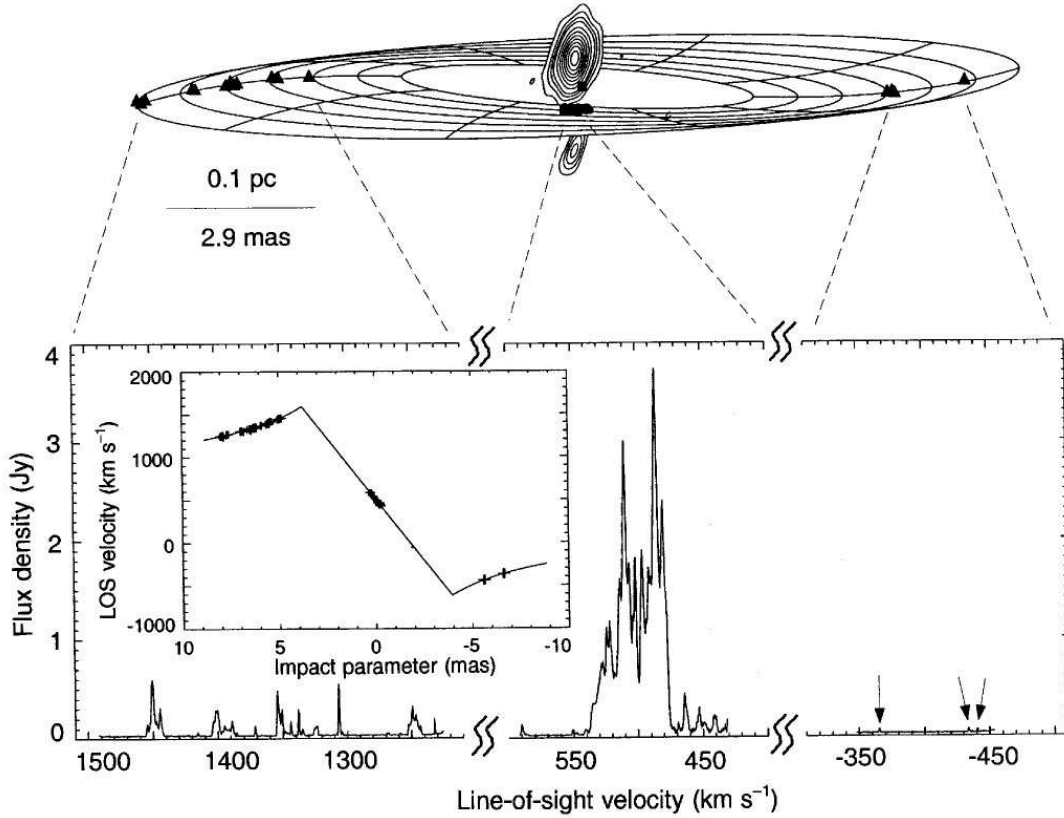
Figure IV.2: Maser orbits fit to a warped disk for NGC4258. Masers can also be useful for distance determinations. Here, the positions and velocities of water masers are able to be fit to a warped disk model surrounding a supermassive black hole. This allows the interpolation of physical radii away from the black hole, giving us both the black hole mass and an standard ruler to allow precise determination of the distance to NGC4258. (Herrnstein et al., 1999)

Stellar dynamics and gas dynamics both probe light coming from matter near the black hole. The width of broadened spectral lines from either the stars or gas can be used to determine a velocity dispersion for the matter local to the SMBH. This velocity dispersion, therefore, can then be used to determine the potential through which the matter is traveling, and thus the mass of the black hole.

A special case of stellar dynamics for which the orbits of the constituent stars can be resolved—namely, for the case of our own Milky Way—adds another dimension to our knowledge of the stellar orbits. Over time, we can observe the proper motion on the sky for these orbits. Combining these measurements with Doppler measurements for radial

velocity yields full orbital solutions. Then, it simply requires Kepler's laws to determine the mass of the SMBH.

Reverberation mapping can be thought of as "echo-mapping" the gas disk around a SMBH. Continuum emission very near the black hole travels outward and stimulates broad line emission in surrounding gas. Any changes in the continuum emission will take time to propagate to the broad line region, since the speed of light is finite. By measuring the timing difference in the change in continuum emission and change in stimulated broad line emission, the physical distance from the SMBH to the broad line region can be inferred. With this radius, and the velocity of the gas in the broad line region measured by the width of the broadened lines, a black hole mass can be determined (Blandford & McKee, 1982).

IV.1.3   Correlations

Correlations between varying properties of galaxies and black holes can provide much deeper insight into the dynamics that shape the evolution of both. Of particular interest here are the fundamental plane of elliptical galaxies, the $M - \sigma$ relation, and the green valley-AGN relation.

IV.1.3.1   The M-Sigma Relation

If we consider the all the observable properties of a galaxy and compare them to the mass of its SMBH, the tightest correlation can be found with the velocity dispersion σ of the galaxy's bulge. Such a tight correlation is surprising, as the sphere of influence of a typical SMBH does not extend much past order a few pc, while bulges exist on scales of a kpc or greater. In essence, the supermassive black hole and the outer edges of the bulge shouldn't "feel" each other. Nevertheless, the correlation is indeed there, suggesting some mechanism that influences—or is influenced by—both of them. Gültekin et al. (2009) use a sample of 49 M_{BH} measurements and 19 upper limits to measure this correlation, and find $\log(M_{BH}/M_\odot) = \alpha + \beta \log(\sigma/200 \text{ km s}^{-1})$ with $(\alpha, \beta, \varepsilon_0) = (8.12 \pm 0.08 M_\odot, 4.24 \pm 0.41 M_\odot, 0.44 \pm 0.06 M_\odot)$ for all galaxies and $(\alpha, \beta, \varepsilon_0) = (8.23 \pm 0.08 M_\odot, 3.96 \pm 0.42 M_\odot, 0.31 \pm$

0.06$M_\odot$) for ellipticals, where ε_0 is the intrinsic scatter in the relation.
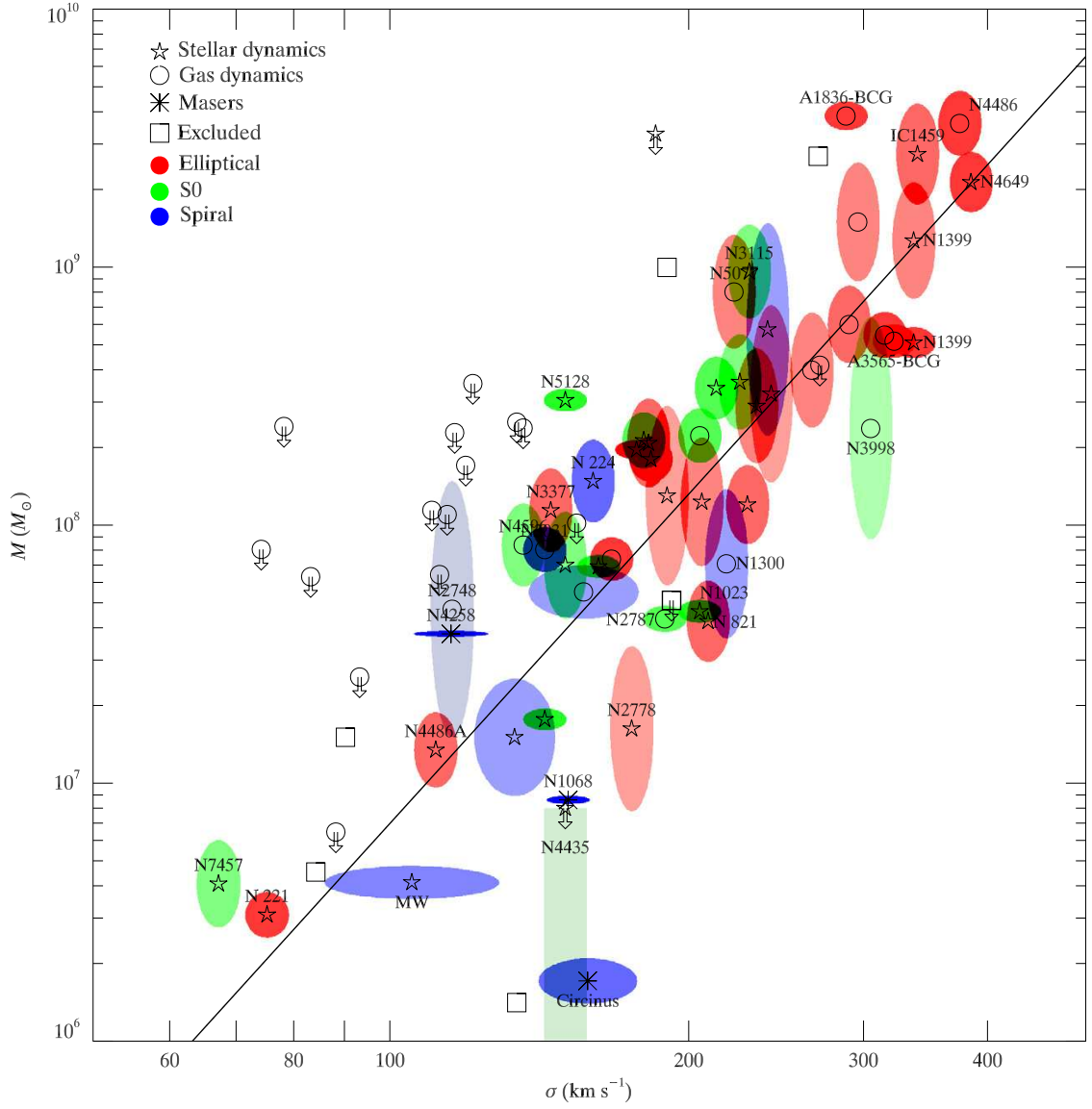
Figure IV.3: The M-σ relation for galaxies with dynamical measurements. Black hole mass is plotted vs velocity dispersion of its host spheroid. The symbols represent the method by which the black hole mass was measured: pentagrams for stellar dynamics, circles for gas dynamics, and asterisks for masers. Upper limits are given by arrows. Error ellipses are colored by galaxy type, with red for ellipticals galaxies, green for lenticular galaxies, and blue for spiral galaxies. The saturation of the color is inversely proportional to the area of the ellipse. For this sample, the best fit relation is $M_{BH} = 10^{8.12}$ $M_\odot(\sigma/200$ km s$^{-1})^{4.24}$. Galaxies not included in this fit are labeled as squares. (Gültekin et al., 2009)

IV.1.3.2 The Fundamental Plane

While not a direct correlation with the properties of supermassive black holes, the fundamental plane of elliptical galaxies offers insight into the characteristics of their hosts. The fundamental plane is a three-parameter correlation between properties of elliptical galaxies: velocity dispersion, effective radius, and surface brightness. This correlation (Figure IV.4) between these three parameters is tighter than the combination of any two alone (Djorgovski & Davis, 1987). The fit for this correlation can be given as $\log R_e = 0.36(\langle I \rangle_e / \mu_B) + 1.4 \log \sigma_0$, where R_e is the effective radius in kpc, $\langle I \rangle_e$ is the mean surface brightness interior to R_e in units of μ_B, and σ_0 is the velocity dispersion in km s^{-1} (Binney & Merrifield, 1998).
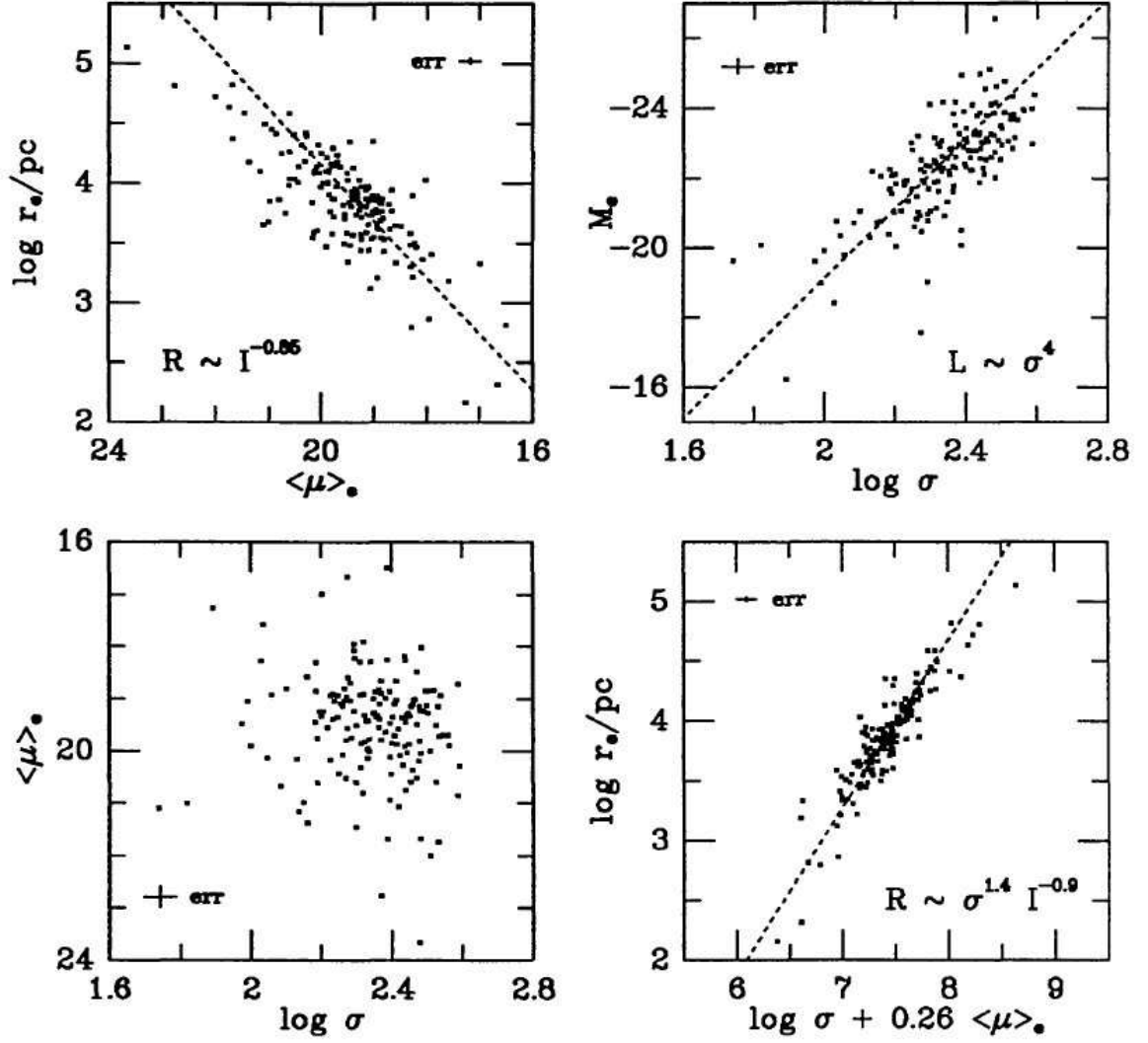
Figure IV.4: The fundamental plane for elliptical galaxies. *Top panels:* The top panels show the one-parameter scaling relations, with the relation between radius and mean surface brightness on the left and the relation between luminosity and velocity dispersion (the Faber-Jackson relation) on the right. *Bottom left:* The relation between the surface brightness and velocity dispersion. This is an almost face-on view of the fundamental plane. *Bottom right:* The relation between the effective radius and the combination of surface brightness and velocity dispersion. This is the edge-on view of the fundamental plane. (Kormendy & Djorgovski, 1989)

IV.1.3.3 The Green Valley

When considering both the color and stellar mass of a galaxies, a correlation emerges where many galaxies lie in either the "blue cloud" of bluer, lower mass galaxies, or the "red

sequence" of redder, generally higher mass galaxies. The area between these two is known as the "green valley" and, while not as populated as the blue cloud or red sequence, holds special interest when active galactic nuclei (AGN) are considered. AGN are very luminous regions at the centers of some galaxies. Schawinski et al. (2010) show that galaxies falling on the green valley are much more likely to host AGN than galaxies on the blue cloud or red sequence, hinting at an underlying link between the evolution of galaxies, and the activity at their centers.
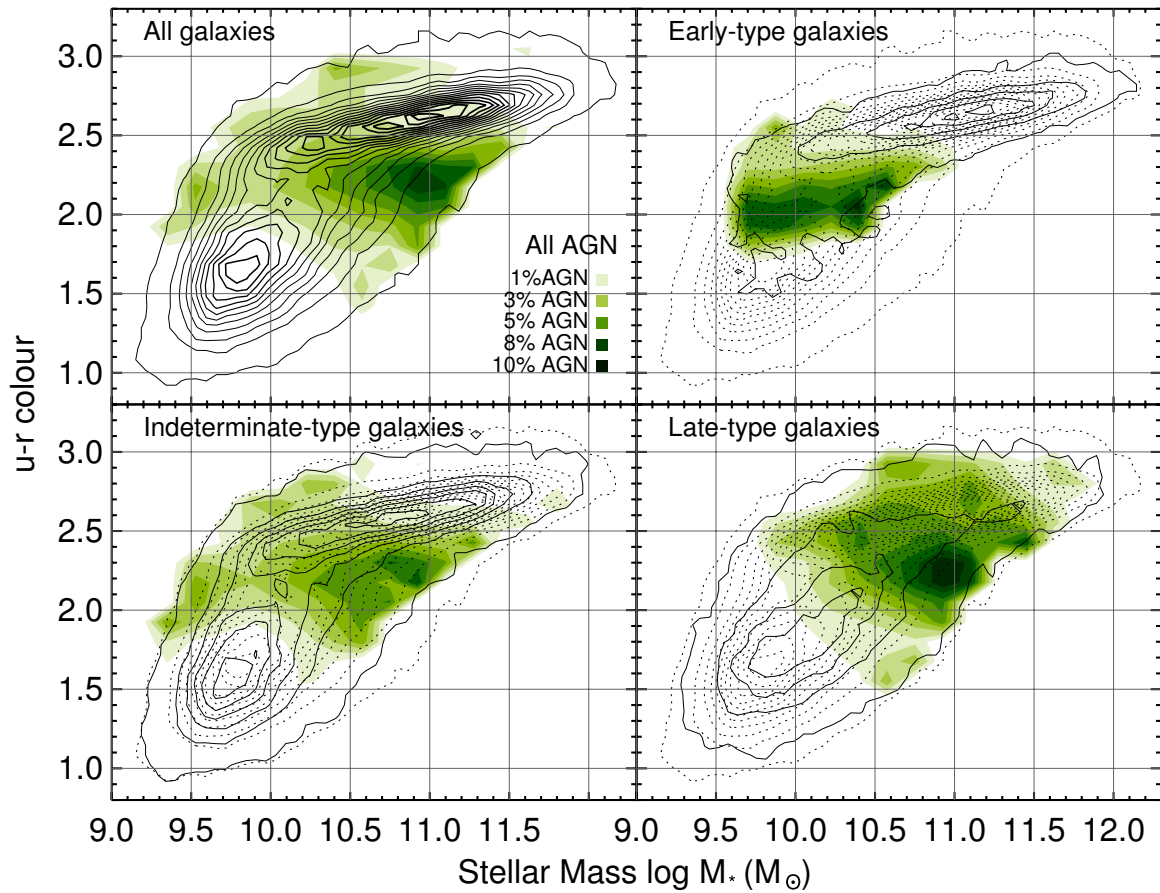
Figure IV.5: Distribution of the fraction of galaxies containing AGN. Galaxy color in u-r is plotted vs stellar mass. The contours are the galaxy population for all galaxies (top-left), early-type galaxies (top right), intermediate-type galaxies (bottom left), and late type galaxies (bottom right). For the three sub-samples, dotted contours represent the full sample for comparison. The green shaded contours represent the fraction of galaxies in that subsample that contain active galactic nuclei. It can be clearly seen that the AGN fraction is highest for galaxies falling within the green valley. (Schawinski et al., 2010)

IV.2 Galaxy Evolution

IV.2.1 Dark Matter Halos

Every galaxy resides inside a dark matter halo. Often about an order of magnitude larger in both radius and mass than the baryonic component, dark mater halos dominate the large-scale behavior of galaxies. Dark matter is matter that is thought to interact very weakly or not at all with light and ordinary matter, except gravitationally. Evidence for dark matter comes from a number of sources, including the relatively flat rotational velocity curve of galaxies, the velocity dispersion of galaxies, gravitational lensing measurements, galaxy clustering, and the offset between the gas and dominant mass measured in the Bullet cluster. Here we will briefly discuss the evidence from flat rotation curves.

If there were no dark matter component and only the baryonic components (i.e. stars and gas) contributed to the galactic potential, we would expect the rotational velocity of galaxies to fall off with radius. However, observations show that the rotation curve remains relatively flat (Rubin et al., 1980). Figure IV.6 shows several observed rotation curves.

Figure IV.6: Rotation curves for 21 Sc galaxies. It is readily identifiable that the rotation curves do not fall off as would be expected for galaxies without a dark matter component. (Rubin et al., 1980)

Navarro et al. (1997b) found that dark matter halos generally follow the same density
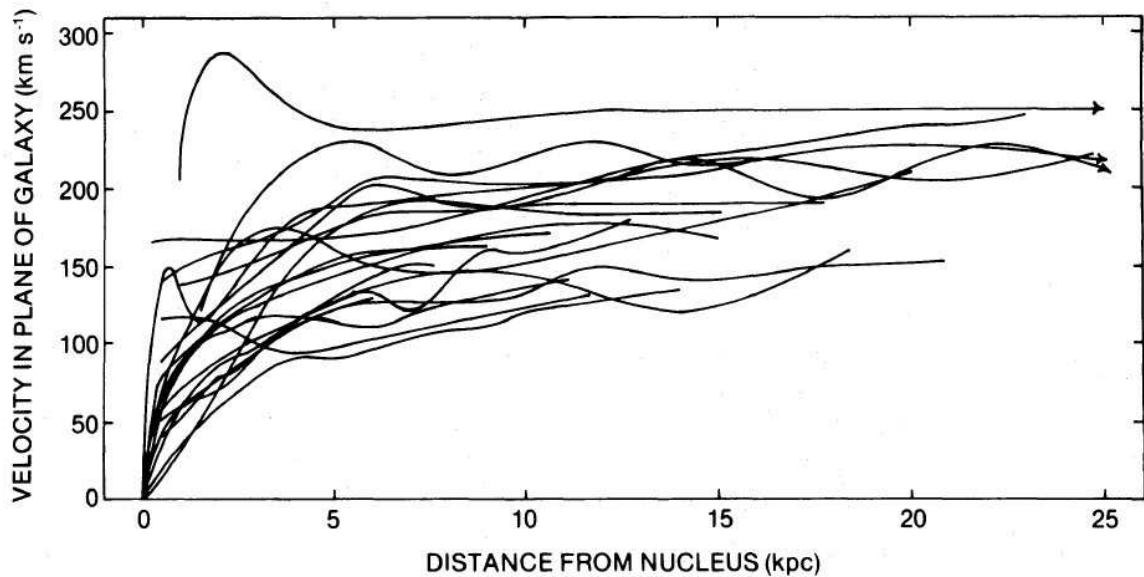
profile, regardless of mass. This universal dark matter density profile can be given as

$$\rho(r) \propto \frac{1}{(r/a)(1+r/a)^2},$$ (IV.1)

where a is the radius where the profile transitions from an r^{-1} power law to an r^{-3} power law.

IV.2.2 Galaxy Mergers

Galaxy mergers are the fundamental mechanism by which galaxies grow and evolve. Collisions between galaxies trigger processes that can alter nearly all the properties of the galaxies. Naturally, mergers increase the mass of galaxies. Starting from small perturbations in the early universe, gravity slowly pulls matter together to form larger and larger clumps. These clumps of gas and dark matter eventually form stars, beginning what we think of as typical galaxies, and over time, these galaxies merge together into larger and larger galaxies.

Mergers affect many other properties of galaxies as well. Mergers distort the shapes of galaxies, causing long tidal tails to form and the entire morphology to appear irregular. The disk structures of spiral galaxies that form from the settling of the rotational component are distorted and "puffed up" into components with ever increasing bulge-like properties.

Mergers can trigger wide-scale starburst events, where a large portion of gas goes into the formation of stars. Much of the gas component of the galaxy can subsequently be blown out by the winds from the supernovae of short-lived O and B stars. This shuts off star formation, and as the stellar population is no longer replenished with new high-mass stars, the galaxy becomes progressively redder as large stars die.

The general trend is for mergers to move galaxies from the right side of the Hubble tuning fork towards the left, turning blue, gas rich spirals into red, gas poor ellipticals. This process is aided by the AGN feedback also triggered during galaxy mergers, as we discuss in the following section.

39

IV.3 Supermassive Black Hole Growth

Supermassive black holes grow by two primary mechanisms, binary mergers and gas accretion. Through a combination of these, black holes can grow to as large as $\sim 10^9$–10^{10} M$_\odot$ by $z = 0$.

IV.3.1 Binary Mergers

When two galaxies merge, the supermassive black holes at their hearts begin a process that will eventually lead to their coalescence. There are generally thought to be three stages to this journey. First, the black holes sink towards the center of the merged galaxy through mass segregation and dynamical friction until they form a bound orbit with each other. Then, the black holes tighten their orbit through three-body scattering of nearby stars. Finally, as the black holes become close enough together for general relativistic effects to come into play, gravitational waves are emitted and radiate away the remaining orbital energy until the binary coalesces.

IV.3.1.1 Dynamical Friction and Inspiral

During the majority of the inspiral process, the black holes do not "feel" each other's gravitational pull. Instead, interactions with the galaxy itself push the holes together.

As it travels through a galaxy, a black hole—or any massive body—is slowed by the surrounding field of matter. Gravitational attraction pulls surrounding matter toward the black hole. However, as the black hole is moving with respect to the local medium, the attracted particles will tend to fall behind the black hole. This creates a wake of overdensity that gravitationally attracts the black hole from behind and slows its velocity. Chandrasekhar (1943) develops this notion of dynamical friction for the motion of a star through a sea of other stars. If the distribution of velocities of the surrounding particles is Maxwellian, the acceleration on the black hole can be written as

$$\frac{d\mathbf{v}_M}{dt} = -\frac{4\pi G^2 M \rho \ln \Lambda}{v_M^3} \left[\mathrm{erf}(X) - \frac{2X}{\sqrt{\pi}} e^{-X^2} \right] \mathbf{v}_M, \qquad \text{(IV.2)}$$

where $\mathbf{v}_M$ is the velocity of the black hole, M is it's mass, ρ is the density of surrounding matter, erf is the error function, $\ln\Lambda$ is the Coulomb logarithm, and $X \equiv v_M/(\sqrt{2}\sigma)$ where σ is the velocity dispersion of the surrounding medium (Binney & Tremaine, 1988). As the black hole is slowed by dynamical friction, it loses angular momentum and sinks towards the center of the galaxy's potential well.

IV.3.1.2   The Final Parsec Problem

Dynamical friction and mass segregation can only take us so far. Once the black holes are close enough together, they form a bound binary orbit. This generally occurs for separations of around a few to tens of parsecs. This presents a problem, however, since the orbit needs to shrink to around 10^{-2}–10^{-3} pc in order for gravitational wave emission to remove energy from the orbit in a significant amount. The orbit can be tightened with three-body scattering of stars that wander through the orbit of the binary, however, in the spherical galaxies where mergers often take place, there is a depletion of stars with orbits that intersect the binary. Khan et al. (2011), however, show that the non-spherical, triaxial potential typical of post-merger galaxy remnants can efficiently funnel stars through the orbit of the black hole binary with sufficient intensity to tighten the binary orbit to the gravitational wave regime.

IV.3.1.3   Gravitational Waves and Recoil Kicks

Once the black hole binary separation reaches the point where strong field general relativistic effects come into play, we no longer require external influences to nudge the black holes together. In the final plunge toward coalescence, the black hole binary sheds energy through emission of gravitational radiation. As energy is radiated away, the binary tightens its orbit until the two black holes merge into one. Following this coalescence, the resultant black hole undergoes a "ringdown" phase, in which the distorted space time settles back down into a black hole that can again be simply described by mass, charge, and spin.

The emission of gravitational waves has two interesting consequences. First, the radiation from two merging supermassive black holes is extremely loud, and can potentially

provide an observational signature of the process for gravitational wave observatories. Second, the gravitational waves carry linear momentum, leading to a recoil "kick" imparted to the black hole merger remnant.

Recent advances in numerical relativity simulations have provided a much deeper insight into the black hole binary merger process than has been previously available. Waveforms produced from these simulations (Figure IV.7) can be used to predict what gravitational wave observatories such as LIGO and LISA would expect to observe for signals originating from merging supermassive black hole binaries. Having these waveforms as templates for comparison to data can greatly increase the signal to noise ratio for these detectors, potentially allowing the gravitational wave events to be seen among the sea of noise. These waveforms produced from simulations of the last few orbits of inspiral through the merger and ringdown can be combined with waveforms suggested from post-Newtonian approximations for the longer duration inspiral to provide a complete extended signal to match against.
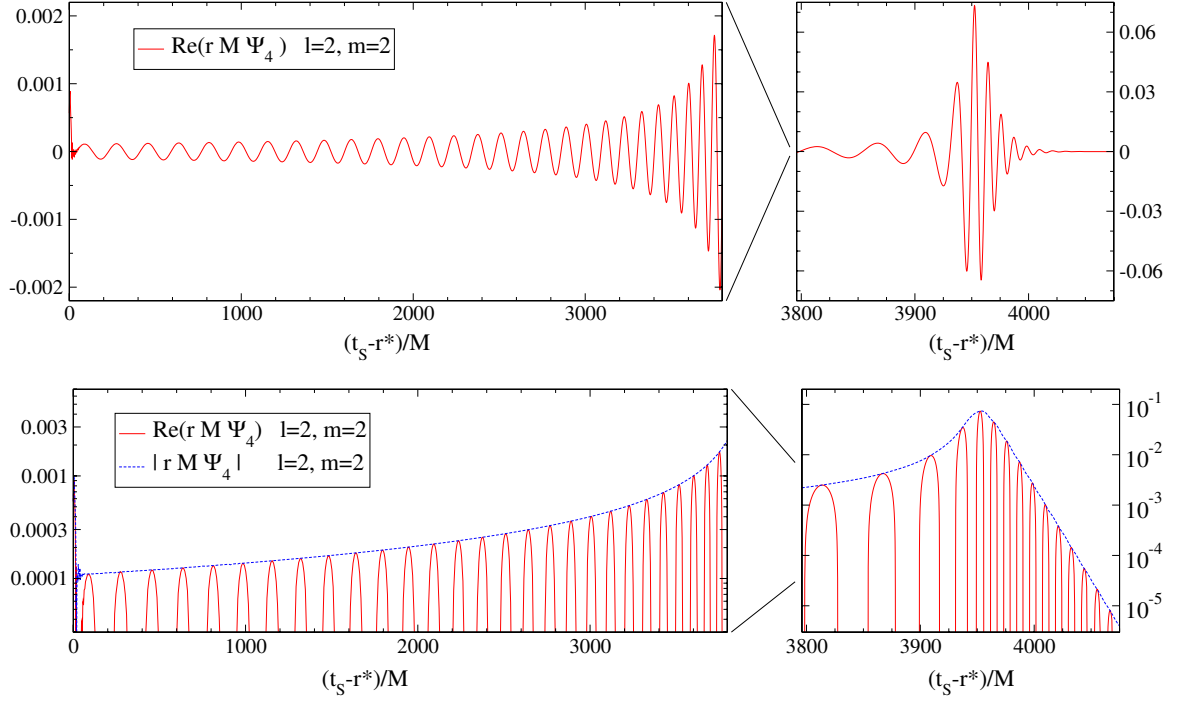
Figure IV.7: Gravitational waveform for an equal-mass, non-spinning black hole binary merger. This is the final waveform, extrapolated to infinity, from the numerical relativity simulation of Scheel et al. (2009). The waveform is shown on the top panel with a linear y-axis and on the bottom panel with a logarithmic y-axis. The left panels are the earlier stages of inspiral, and the right panels show the merger and ringdown stages.

For asymmetric mergers, gravitational radiation is emitted anisotropically. This causes a recoil kick, in which the gravitational waves impart a net velocity to the final black hole with respect to the original center of mass. The magnitude and direction of this kick are dependent on the mass ratio of the binary and the spins of the two black holes—in all, a 7-dimensional parameter space. This large parameter space has been largely explored with numerical relativistic simulations, and analytic equations can be fit to the data to predict the recoil from a given merger configuration. Holley-Bockelmann et al. (2008), give these equations as

$$\mathbf{v}_{kick} = (1+e)\left[\hat{\mathbf{x}}(v_m + v_\perp \cos\xi) + \hat{\mathbf{y}}v_\perp \sin\xi + \hat{\mathbf{z}}v_\parallel\right],\tag{IV.3}$$

where

$$v_m = A \frac{q^2(1-q)}{(1+q)^5} \left[1 + B \frac{q}{(1+q)^2} \right],$$ (IV.4)

$$v_\perp = H \frac{q^2}{(1+q)^5} \left(\alpha_2^\parallel - q\alpha_1^\parallel \right),$$ (IV.5)

$$v_\parallel = K \cos(\Theta - \Theta_0) \frac{q^2}{(1+q)^5} \left(\alpha_2^\perp - q\alpha_1^\perp \right).$$ (IV.6)

Here, the fitting constants are $A = 1.2 \times 10^4$ km s^{-1}, $B = -0.93$, $H = (7.3 \pm 0.3) \times 10^3$ km s^{-1}, and $K = (6.0 \pm 0.1) \times 10^4$ km s^{-1}. The $\hat{z}$ unit vector is in the direction of the orbital angular momentum, and $\perp$ and $\parallel$ refer to components perpendicular and parallel to $\hat{z}$, respectively. The fitting parameters are the eccentricity e, the mass ratio $q \equiv M_2/M_1$, and the reduced spin parameters $\alpha_i \equiv S_i/M_i^2$ where S is the spin angular momentum. The orientation of the merger is given by the angles Θ, Θ_0, and ξ (Holley-Bockelmann et al., 2008).

Slices through this parameter space are shown in Figure IV.8. For certain configurations of the merger, the recoil velocity can be very high. Very asymmetric mergers can produce recoils as high as ~ 4000 km s^{-1}. These large recoils can be enough for the black hole to escape the potential well of its host galaxy and be ejected. Even less extreme recoil kicks can affect the evolution of black holes, as the kicked black hole can oscillate about its host's center, potentially changing its local gas environment and accretion rate.
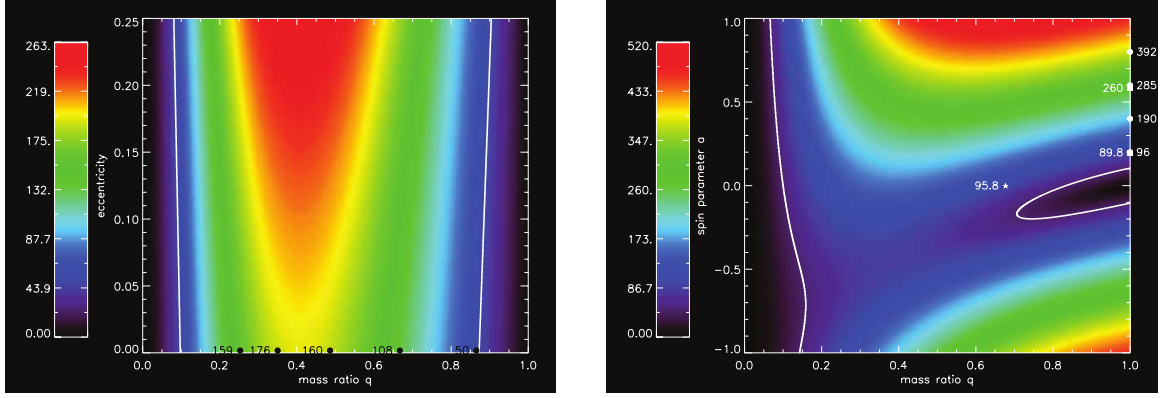
Figure IV.8: *Left:* Gravitaional wave recoil velocity from a merger of nonspinning black holes as a function of eccentricity and mass ratio. Data from numerical relativity simulations (González et al., 2007) are overlaid along the zero eccentricity line. The overlaid white contours are the escape velocity of a typical globular cluster, 50 km s^{-1}. *Right:* Gravitational wave recoil kick velocity as a function of spin parameter and mass ratio for a merger of spinning black holes on a circular orbit with spins perpendicular to the orbital plane of the binary and anti-aligned with each other. Again, the 50 km s^{-1} escape velocity of a globular cluster is overlaid as white contours. Results from numerical relativity simulations are over-plotted: squares for Koppitz et al. (2007), cirlces for Herrmann et al. (2007), and star for Brügmann et al. (2004). (Holley-Bockelmann et al., 2008)

IV.3.2   Accretion

Although mergers play an important role in the evolution of supermassive black holes, gas accretion can often dominate in terms of mass growth. Gas can fall into a black hole in a number of ways. Here, we will discuss accretion onto a moving black hole, spherical accretion onto a stationary black hole, and disk accretion onto a stationary black hole.

IV.3.2.1   Bondi-Hoyle-Lyttleton Accretion

Let us first consider a massive object, in this case our black hole, moving through a uniform density gas medium. Just as in the case of dynamical friction, particles close enough to the black hole will feel a gravitational attraction, causing them to move toward the black hole. As they move closer, the black hole is also moving through the medium, causing the gas particles to focus behind the black hole. As the particle stream reaches the wake directly

behind the black hole, it collides with opposing streams, causing the angular momentum to go to zero. If these particles are bound, they will proceed to fall onto the black hole. Hoyle & Lyttleton (1939) derive an impact parameter for which particles will be accreted,

$$\sigma < \sigma_{HL} = \frac{2GM}{v_\infty^2}, \tag{IV.7}$$

and a mass accretion from the wake column at a rate of

$$\dot{M}_{HL} = \pi \sigma_{HL}^2 v_\infty \rho_\infty = \frac{4\pi G^2 M^2 \rho_\infty}{v_\infty^3}, \tag{IV.8}$$

where v_∞ and ρ_∞ are the velocity and density far away from the black hole, respectively. Expanding upon this analysis, Bondi & Hoyle (1944) suggest that the accretion rate should rather be

$$\dot{M}_{BH} = \frac{2\alpha\pi G^2 M^2 \rho_\infty}{v_\infty^3}, \tag{IV.9}$$

where α is a constant between 1 and 2, with a typical value of around 1.25.

For an accretor at rest in an isotropic gas medium, one would expect accretion to be a spherical process. Bondi (1952) considers this configuration, and finds the accretion rate for this "temperature-limited" case to be

$$\dot{M}_{Bondi} = \frac{2\pi G^2 M^2 \rho_\infty}{c_{s,\infty}^3}, \tag{IV.10}$$

where $c_{s,\infty}$ is the speed of sound far away from the black hole.

Extrapolating between this result and the "velocity-limited" case of Equation IV.9 suggests (Bondi, 1952)

$$\dot{M}_{BH} = \frac{2\pi G^2 M^2 \rho_\infty}{\left(c_{s,\infty}^2 + v_\infty^2\right)^{3/2}} \tag{IV.11}$$

as an order of magnitude estimate of the more general case of accretion. Numerical simulations (Shima et al., 1985) suggest an additional factor of 2 is needed for better agreement

46

with simulation results, giving us a generally applicable from for the accretion rate,

$$\dot{M}_{BH} = \frac{4\pi G^2 M^2 \rho_\infty}{\left(c_{s,\infty}^2 + v_\infty^2\right)^{3/2}}.$$ (IV.12)

IV.3.2.2 Disk Accretion and Active Galactic Nuclei

Active galactic nuclei play a fundamental role in the evolution of both supermassive black holes and their host galaxies. As gas falls in to a black hole in the center of a galaxy, its angular momentum forces it into an accretion disk. As matter moves towards the SMBH, it transfers its gravitational potential energy to thermal energy. For accretion disks around supermassive black holes, this can cause the disk to emit large amounts of electromagnetic radiation (Lin & Papaloizou, 1996).

This emitted radiation is important in a number of ways. Most critical to the SMBH itself is the radiation pressure exerted on infalling matter. This radiation pressure sets an upper limit on the rate of accretion, as there is a point where the force from emitted radiation balances the force of gravity for infalling gas (Rybicki & Lightman, 1979). This limit, known as the Eddington limit, is given by

$$L_{Edd} = 4\pi GMcm_H/\sigma_T = 1.25 \times 10^{38} \text{erg s}^{-1}(M/M_\odot),$$ (IV.13)

where c is the speed of light, m_H is the mass of hydrogen, and σ_T is the Thompson cross section.

The radiation given off by the accretion disk affects galactic properties as well. Powerful AGN can strip away gas from the center of the galaxy, halting star formation. This can quickly change a galaxy from a blue, gaseous, star forming galaxy into one that is red, dry, and dead.

IV.4   Conclusion

We have seen that galaxies and the supermassive black holes at their centers both have their most dramatic periods of evolution around the same time. Galaxy mergers grow both the galaxy and the SMBH. Galaxies grow and become more elliptical as mergers bring in additional mass on orbits that can disrupt their gaseous disks. These mergers also bring in counterpart supermassive black holes that fall toward the center of the galaxy and merge with the central SMBH, while also triggering accretion events and AGN feedback that pump energy back into the galaxy, shutting off star formation.

IV.4.1   Correlations

In light of these shared growth mechanisms, the correlations mentioned in Section IV.1 begin to move from a purely observational coincidence to a natural result of co-evolution. The M–σ relation is a natural byproduct of the simultaneous growth of supermassive black holes and their galaxies during merger events. The mass of the SMBH increases due to the merging of binary companions and increased levels of accretion, while the host mass, and thus velocity dispersion, increases due to the infalling galaxy itself. Likewise, the over-abundance of AGN in galaxies lying in the green valley is the consequence of simultaneous change. Mergers both trigger highly luminous AGN feedback and cause an inexorable shift from the blue cloud, through the green valley, to the red sequence. Even the increase in scatter of the M–σ relation at low masses can be explained by the galaxies having lower mass, and therefore being more likely to allow a gravitational wave recoil kicked black hole of a given velocity to escape.

IV.4.2   Open Questions

In the end, there remain a number of open questions. How can very large supermassive black holes form so early? What is dark matter actually made of? How do galaxies retain their black holes if merger recoils can kick them with velocities greater than the escape velocity of the galaxy? Over what range are our correlations truly valid? These are just

some of the questions that are currently being investigated, and promise to provide a rich field of study for years to come.

CHAPTER V

Conclusion

BIBLIOGRAPHY

Alvarez, M. A., Wise, J. H., & Abel, T. 2009, Astrophys. J., Lett., 701, L133

Behroozi, P. S., Wechsler, R. H., & Wu, H.-Y. 2013, Astrophys. J., 762, 109

Binney, J., & Merrifield, M. 1998, Galactic Astronomy, Princeton Series in Astrophysics (Princeton University Press)

Binney, J., & Tremaine, S. 1988, Galactic Dynamics, Princeton Series in Astrophysics (Princeton University Press)

Blandford, R. D., & McKee, C. F. 1982, Astrophys. J., 255, 419

Bondi, H. 1952, Mon. Not. R. Astron. Soc., 112, 195

Bondi, H., & Hoyle, F. 1944, Mon. Not. R. Astron. Soc., 104, 273

Bouchet, F. R., Colombi, S., Hivon, E., & Juszkiewicz, R. 1995, Astron. Astrophys., 296, 575

Brügmann, B., Tichy, W., & Jansen, N. 2004, Phys. Rev. Lett., 92, 211101

Bryan, G. L., & Norman, M. L. 1998, Astrophys. J., 495, 80

Buchert, T. 1994, Mon. Not. R. Astron. Soc., 267, 811

Buchert, T., Melott, A. L., & Weiss, A. G. 1994, Astron. Astrophys., 288, 349

Bullock, J. S., Kolatt, T. S., Sigad, Y., et al. 2001, Mon. Not. R. Astron. Soc., 321, 559

Chandrasekhar, S. 1943, Astrophys. J., 97, 255

Couchman, H. M. P., & Rees, M. J. 1986, Mon. Not. R. Astron. Soc., 221, 53

Crocce, M., Pueblas, S., & Scoccimarro, R. 2006, Mon. Not. R. Astron. Soc., 373, 369

Davis, M., Efstathiou, G., Frenk, C. S., & White, S. D. M. 1985, Astrophys. J., 292, 371

Djorgovski, S., & Davis, M. 1987, Astrophys. J., 313, 59

Efstathiou, G., Davis, M., White, S. D. M., & Frenk, C. S. 1985, Astrophys. J., Suppl. Ser., 57, 241

Einasto, J., Klypin, A. A., Saar, E., & Shandarin, S. F. 1984, Mon. Not. R. Astron. Soc., 206, 529

Eke, V. R., Navarro, J. F., & Steinmetz, M. 2001, Astrophys. J., 554, 114

Gao, L., Navarro, J. F., Cole, S., et al. 2008, Mon. Not. R. Astron. Soc., 387, 536

González, J. A., Sperhake, U., Brügmann, B., Hannam, M., & Husa, S. 2007, Phys. Rev. Lett., 98, 091101

Gültekin, K., Richstone, D. O., Gebhardt, K., et al. 2009, The Astrophysical Journal, 698, 198

Heger, A., Fryer, C. L., Woosley, S. E., Langer, N., & Hartmann, D. H. 2003, Astrophys. J., 591, 288

Heitmann, K., Lukić, Z., Habib, S., & Ricker, P. M. 2006, Astrophys. J., Lett., 642, L85

Herrmann, F., Hinder, I., Shoemaker, D., Laguna, P., & Matzner, R. A. 2007, Astrophys. J., 661, 430

Herrnstein, J. R., Moran, J. M., Greenhill, L. J., et al. 1999, Nature, 400, 539

Holley-Bockelmann, K., Gültekin, K., Shoemaker, D., & Yunes, N. 2008, Astrophys. J., 686, 829

Holley-Bockelmann, K., Wise, J. H., & Sinha, M. 2012, Astrophys. J., Lett., 761, L8

Hoyle, F., & Lyttleton, R. A. 1939, Proceedings of the Cambridge Philosophical Society, 35, 405

Hubble, E. P. 1926, Astrophys. J., 64, 321

Islam, R. R., Taylor, J. E., & Silk, J. 2003, Mon. Not. R. Astron. Soc., 340, 647

Jenkins, A. 2010, Mon. Not. R. Astron. Soc., 403, 1859

Jeon, M., Pawlik, A. H., Greif, T. H., et al. 2012, Astrophys. J., 754, 34

Khan, F. M., Just, A., & Merritt, D. 2011, Astrophys. J., 732, 89

Klypin, A. A., & Shandarin, S. F. 1983, Mon. Not. R. Astron. Soc., 204, 891

Klypin, A. A., Trujillo-Gomez, S., & Primack, J. 2011, Astrophys. J., 740, 102

Koppitz, M., Pollney, D., Reisswig, C., et al. 2007, Phys. Rev. Lett., 99, 041102

Kormendy, J., & Djorgovski, S. 1989, Ann. Rev. Astron. Astrophys., 27, 235

Lin, D., & Papaloizou, J. 1996, Annual Review of Astronomy and Astrophysics, 34, 703

Lo, K. Y. 2005, Ann. Rev. Astron. Astrophys., 43, 625

Lukić, Z., Heitmann, K., Habib, S., Bashinsky, S., & Ricker, P. M. 2007, Astrophys. J., 671, 1160

Macciò, A. V., Dutton, A. A., & van den Bosch, F. C. 2008, Mon. Not. R. Astron. Soc., 391, 1940

Madau, P., & Rees, M. J. 2001, Astrophys. J., Lett., 551, L27

Micic, M., Holley-Bockelmann, K., & Sigurdsson, S. 2011, Mon. Not. R. Astron. Soc., 414, 1127

Muñoz-Cuartas, J. C., Macciò, A. V., Gottlöber, S., & Dutton, A. A. 2011, Mon. Not. R. Astron. Soc., 411, 584

Nadarajah, S. 2005, Journal of Applied Statistics, 32, 685

Navarro, J. F., Frenk, C. S., & White, S. D. M. 1996, Astrophys. J., 462, 563

—. 1997a, Astrophys. J., 490, 493

—. 1997b, Astrophys. J., 490, 493

Neto, A. F., Gao, L., Bett, P., et al. 2007, Mon. Not. R. Astron. Soc., 381, 1450

Prada, F., Klypin, A. A., Cuesta, A. J., Betancort-Rijo, J. E., & Primack, J. 2012, Mon. Not. R. Astron. Soc., 423, 3018

Press, W. H., & Schechter, P. 1974, Astrophys. J., 187, 425

Reed, D. S., Bower, R., Frenk, C. S., Jenkins, A., & Theuns, T. 2007, Mon. Not. R. Astron. Soc., 374, 2

Rubin, V. C., Ford, W. K. J., & . Thonnard, N. 1980, Astrophys. J., 238, 471

Rybicki, G. B., & Lightman, A. P. 1979, Radiative processes in astrophysics / George B. Rybicki, Alan P. Lightman (Wiley, New York :), xv, 382 p. :

Schawinski, K., Urry, C. M., Virani, S., et al. 2010, The Astrophysical Journal, 711, 284

Scheel, M. A., Boyle, M., Chu, T., et al. 2009, Phys. Rev. D, 79, 024003

Scoccimarro, R. 1998, Mon. Not. R. Astron. Soc., 299, 1097

Shima, E., Matsuda, T., Takeda, H., & Sawada, K. 1985, Mon. Not. R. Astron. Soc., 217, 367

Sinha, M., & Holley-Bockelmann, K. 2009, Mon. Not. R. Astron. Soc., 397, 190

—. 2010, Mon. Not. R. Astron. Soc., 405, L31

Sirko, E. 2005, Astrophys. J., 634, 728

Springel, V. 2005, Mon. Not. R. Astron. Soc., 364, 1105

Springel, V., Yoshida, N., & White, S. D. M. 2001, New Astron, 6, 79

Tanaka, T., & Haiman, Z. 2009, Astrophys. J., 696, 1798

Tegmark, M., Silk, J., Rees, M. J., et al. 1997, Astrophys. J., 474, 1

Voit, G. M. 2005, Reviews of Modern Physics, 77, 207

Volonteri, M., Haardt, F., & Madau, P. 2003, Astrophys. J., 582, 559

Wechsler, R. H., Bullock, J. S., Primack, J. R., Kravtsov, A. V., & Dekel, A. 2002, Astrophys. J., 568, 52

White, M. 2001, Astron. Astrophys., 367, 27

Zel'dovich, Y. B. 1970, Astron. Astrophys., 5, 84

Zhao, D. H., Jing, Y. P., Mo, H. J., & Börner, G. 2009, Astrophys. J., 707, 354

Zhao, D. H., Mo, H. J., Jing, Y. P., & Börner, G. 2003, Mon. Not. R. Astron. Soc., 339, 12